

1 Quantifying Temperature-sliding Inconsistency in Thermomechanical Coupling: A  
2 Comparative Analysis of Geothermal Heat Flux Datasets at Totten Glacier

3  
4 Junshun Wang<sup>1</sup>, Liyun Zhao<sup>1</sup>, Michael Wolovick<sup>2</sup>, John C. Moore<sup>3</sup>

5 <sup>1</sup>State Key Laboratory of Earth Surface Processes and Hazards Risk Governance  
6 (ESPHR), Faculty of Geographical Science, Beijing Normal University, Beijing  
7 100875, China

8 <sup>2</sup>Glaciology Section, Alfred-Wegener-Institut, Helmholtz-Zentrum für Polar- und  
9 Meeresforschung, Bremerhaven, Germany

10 <sup>3</sup>Arctic Centre, University of Lapland, Rovaniemi, Finland

11 *Correspondence: Liyun Zhao ([zhaoliyun@bnu.edu.cn](mailto:zhaoliyun@bnu.edu.cn)), John C. Moore*  
12 *([john.moore.bnu@gmail.com](mailto:john.moore.bnu@gmail.com))*

13  
14  
15  
16 **Abstract.** Rapid sliding of ice sheets requires warm basal temperatures and lubricating  
17 basal meltwater, whereas slow velocities typically correlate with a frozen bed. However,  
18 ice sheet models often infer basal sliding by inverting surface velocity observations  
19 with the vertical structure of temperature and hence rheology held constant. If the  
20 inversion is allowed to freely vary sliding over the model domain, then inconsistencies  
21 between the basal thermal state and ice motion can arise lowering simulation realism.  
22 In this study, we propose a new method that quantifies inconsistencies when inferring  
23 ~~warmthawed~~ and ~~frozoneold~~-bedded regions of ice sheets. This method can be used to  
24 evaluate the quality of ice sheet simulation results without requiring any englacial or  
25 subglacial measurements. We apply the method to evaluate simulation results for Totten  
26 Glacier using an isotropic 3D full-Stokes ice sheet model with eight geothermal heat  
27 flux (GHF) datasets and compare our evaluation results with inferences on basal  
28 thermal state from radar specularity. The rankings of GHF datasets based on  
29 inconsistency are closely aligned with those using the independent specularity content  
30 data. Examples of the method utility are 1. an ~~overcooling~~ inconsistency ~~characterizing~~  
31 ~~overcooling~~ with all GHFs near the western boundary of Totten Glacier between 70°S-  
32 72°S, where there is a bedrock canyon and fast surface ice velocities, ~~which~~ ~~suggestings~~  
33 that ~~all~~ GHFs ~~are~~ ~~is~~ low ~~in all published datasets~~; 2. an overheating inconsistency in the  
34 eastern Totten Glacier with all GHFs ~~suggestingthat leads to~~ overestimation of ice  
35 temperature due, in this case, to an unrealistically warm surface temperature. Our  
36 approach opens a new avenue for assessing the self-consistency and reliability of ice  
37 sheet model results and GHF datasets, which may be widely applicable.

## 38 1. Introduction

39 Ice sheet models are an important tool for projections of ice sheet mass balance  
40 and their contribution to sea level rise. Ice sheet models are usually initialized by “spin-  
41 up” or data assimilation such that they reproduce the present-day geometry or surface  
42 velocity of an ice sheet (Seroussi et al., 2019). Often ice sheet model simulations derive  
43 ice dynamics using ice temperatures taken from other studies (e.g., Gillet-Chaulet et al.,  
44 2012; Van Liefferinge and Pattyn, 2013; Cornford et al., 2015; Pittard et al., 2016;  
45 Siahhaan et al., 2022). In thermo-mechanically coupled ice sheet simulations, the ice  
46 sheet model is usually spun up with idealized temperature-depth profiles and then run  
47 in a thermo-mechanically coupled mode constrained by geothermal heat flux (GHF)  
48 and surface ice temperature fields (Seroussi et al., 2019). While advances in satellite  
49 and field observation technologies have led to a preliminary consensus on ice sheet  
50 geometry and surface ice temperature, significant uncertainties persist in basal  
51 boundary conditions, including GHF and basal friction, since reliable observational  
52 data are scarce. These basal properties introduce significant uncertainty in the simulated  
53 ice sheet dynamics, and thus ice sheet mass balance.

54 The GHF, the heat flow from the Earth's crust to the base of ice sheet, is a critical  
55 variable in the basal boundary condition for simulating the ice temperature profile, and  
56 hence ice rheology and flow dynamics (Fisher et al., 2015; Smith - Johnsen et al., 2020;  
57 Reading et al., 2022). Several GHF datasets exist, derived in various ways from  
58 geophysical observations and models, and they exhibit significant variability in both  
59 spatial distribution and magnitude (e.g., An et al., 2015; Dziadek et al., 2017; Martos et  
60 al., 2017; Shen et al., 2020; Stål et al., 2021). These GHF datasets have been widely  
61 used in thermodynamic simulations of Antarctica (e.g., McCormack et al., 2022;  
62 Shackleton et al., 2023; Park et al., 2024; Van Liefferinge et al., 2018). However,  
63 assessing the GHF field accuracy is problematic because in situ measurements such as  
64 boreholes are sparse. Few studies have assessed the quality and reliability of GHF  
65 datasets over specific regions. Kang et al. (2022) employed a combination of forward  
66 model and inversion using a 3D full-Stokes ice flow model to simulate the basal thermal  
67 state in the Lambert–Amery Glacier region and evaluate different GHFs using the  
68 locations of subglacial lakes, but the constraints used were asymmetric between  
69 coldfrozen and warmthawed beds, and assigned inflated reliability to the warmer GHF  
70 maps. Indirect estimates of basal conditions have used airborne radar specularity  
71 content (Schroeder et al., 2013, 2015; Young et al., 2016) as proxies for basal  
72 wetness/dryness and thermal regime (Dow et al., 2020). Huang et al. (2024) used an  
73 inverse modeling approach similar to that of Kang et al. (2022) for Totten Glacier and  
74 combined this with measured radar specularity content to derive a two-sided constraint  
75 on the basal thermal state in addition to subglacial lakes locations. However, specularity  
76 content is not yet available for many regions of Antarctica.

77 The basal friction field is another poorly known boundary condition in ice sheet  
78 modeling, and a key source of uncertainty in the long-term projection of ice sheets and  
79 glaciers. Although basal slip is crucial to the 3D ice flow, it is difficult to observe.  
80 Several basal sliding parameterizations have been proposed and widely used  
81 (Weertman, 1957; Kamb, 1970; Nye, 1970; Budd et al., 1979; Fowler, 1981; Schoof,  
82 2005; Gagliardini et al., 2007; Gladstone et al., 2014; Tsai et al., 2015; Brondex et al.,  
83 2017, 2019). The linear Weertman basal sliding parameterization is the most widely  
84 used due to its simple form. Given prescribed or modelled ice temperatures and hence  
85 ice viscosity, numerous studies have inferred the spatial distribution of basal friction  
86 coefficient over grounded ice to best match observed present-day surface ice velocities  
87 or ice sheet geometry using snapshot or time-dependent data assimilation and inverse  
88 methods (MacAyeal, 1993; Morlighem et al., 2010; Rignot et al., 2011; Gillet-Chaulet  
89 et al., 2012; Larour et al., 2012; Pollard and DeConto, 2012; Morlighem et al., 2013;  
90 Perego et al., 2014; Pattyn, 2017; Albrecht et al., 2020; Lipscomb et al., 2021; Choi et  
91 al., 2023). However, such inversions typically allow the friction coefficient to vary  
92 freely to match the surface velocity observations. This can potentially lead to conflicts  
93 with the temperature field used during the inversion, which we refer to as  
94 “inconsistencies” in this study. For instance, relatively fast surface ice velocity may  
95 demand basal sliding in areas where the basal temperatures are below the local pressure  
96 melting point. These inconsistencies may be due to unrealistic ice temperatures or a  
97 lack of complete physics in the ice sheet model. However, many studies overlook this  
98 aspect, and use the inversion results to initialize ice sheet dynamics simulations and  
99 estimate glacier mass balance and its contribution to sea level rise (Seroussi et al., 2019;  
100 Peyaud et al., 2020; Schannwell et al., 2020; Payne et al., 2021).

101 To the best of our knowledge, there has been no study of such inconsistencies  
102 between [a sliding inversion and the temperature/rheology field used as an input to that](#)  
103 [inversionsimulated ice temperature and observed surface ice velocity](#). Here we develop  
104 a novel and generally applicable method to estimate this inconsistency without relying  
105 on basal observation data. We utilize the inconsistency of the modelled ice temperature  
106 and observed velocity fields to evaluate the quality of ice flow model results. Notably,  
107 this approach can also serve as a supplementary method for assessing geothermal heat  
108 flux datasets, relying solely on surface ice velocity observations rather than additional  
109 englacial or subglacial data.

110 We apply our method to Totten Glacier, a primary outlet of the Aurora subglacial  
111 basin in East Antarctica (Greenbaum et al., 2015; Pritchard et al., 2009). The Totten  
112 Glacier subregion experienced the largest mass loss among drainage basins in East  
113 Antarctica during the period 1979-2017 and 2003-2020 (Kim et al., 2024; Rignot et al.,  
114 2019) (Fig. 1a). We examine inconsistencies between simulated ice temperature and ice  
115 velocity fields using a 3D full-Stokes model using the various GHFs included in Huang

116 et al. (2024) and use this analysis to rank the reliability of different GHF fields. This  
117 GHF ranking closely resembles that reported by Huang et al. (2024), which used the  
118 agreement between the modelled basal thermal regime and specularly content, which  
119 we take as a validation of the method. Since the new method does not require any  
120 englacial or subglacial data, it can be applied to many glaciers, particularly those  
121 lacking observations. Our approach can provide a swift assessment of the plausibility  
122 of basal temperature and velocity simulated by ice sheet models. Additionally, it can be  
123 effectively utilized to map the spatial distribution of GHF over- or under-estimation.

124

## 125 2. Method

### 126 2.1 Methodology in this study

127 The inconsistencies defined in this study are essentially between ~~the modelled~~  
128 ~~basal thermal state and observed surface ice flow motion~~ a sliding inversion and the  
129 temperature/rheology field used as an input to that inversion. More specifically, the  
130 inconsistencies are between ~~modelled frozen bed and~~ modelled basal sliding (which is  
131 tuned to match the observed fast surface velocity during the inversion) and modelled  
132 frozen bed, and between ~~modelled warm bed and~~ observed slow surface velocity (which  
133 is most likely indicative of a non-slip basal condition) and modelled thawed bed. The  
134 inconsistencies originate from multiple causes, including uncertainties in GHF, surface  
135 ice temperature, ice sheet geometry, bed topography, surface velocity, ice density and  
136 incomplete ice flow mechanics.

137 There is no direct correlation between basal temperature and surface velocity;  
138 rather, they are linked through the basal thermal state - the basal temperature being at  
139 or below the pressure melting point. The ice bottom in the study domain can be  
140 partitioned into ~~warm~~ thawed and ~~frozen~~ cold beds depending on whether the simulated  
141 basal ice temperature reaches the local pressure melting point. To effectively penalize  
142 models exhibiting both localized overheating (bed too warm) and overcooling (bed too  
143 cold), we establish overheating metrics within the ~~warm~~ thawed-bedded region and  
144 overcooling metrics within the ~~cold~~ frozen-bedded region to quantitatively assess the  
145 inconsistency between the simulated temperature and velocity fields. Thus, we provide  
146 two-sided constraints on the temperature field that penalize both too high and too low  
147 ice temperature.

148 Overcooling occurs where basal temperature is underestimated. Crucially, in  
149 regions with relatively fast observed surface velocity, the inverse method nevertheless  
150 yields a nonzero basal velocity — a physically inconsistent result given the cold basal  
151 temperature. When basal ice temperature is below the pressure melting point, the basal  
152 modelled velocity is expected to approach zero. This inconsistency is larger for faster  
153 simulated basal ice speed and for colder simulated basal temperatures. We therefore use  
154 a formula that accounts for both variables to quantify overcooling:

155

$$AOC = (T_{melt} - T_{bm}) \times U_{bm}, \quad (1)$$

156 where  $AOC$  stands for absolute overcooling,  $T_{melt}$  is the basal pressure melting point,  
 157  $T_{bm}$  represents the simulated basal ice temperature and  $U_{bm}$  means the simulated basal  
 158 ice speed.

159 For the overheating metric, since the first term of the right-hand side of Eq. (1)  
 160 becomes zero at a **warmthawed** bed, we cannot use a similar formula as Eq. (1). It is  
 161 not straightforward to quantify the inconsistencies between modelled **warmthawed** bed  
 162 and expected slow basal speed given slow observed surface speed. We note the fact that  
 163 modelled basal sliding speed must remain non-negative. If the ice is warm and soft  
 164 enough to permit deformation such that the modelled surface speed is much faster than  
 165 the observed, then a friction inversion will be ineffective to correct this misfit,  
 166 producing a bias towards positive misfits (i.e., model velocities are too fast) in the  
 167 inversion results. Therefore, we use the positive difference between the simulated  
 168 surface ice speed and the observed speed to calculate the inconsistency caused by the  
 169 overheating effect:

$$170 \quad AOH = \max(0, U_{sm} - U_{obs}), \quad (2)$$

171 where  $AOH$  refers to absolute overheating,  $U_{sm}$  represents the modelled surface ice  
 172 speed and  $U_{obs}$  is the observed surface ice speed. We only calculated  $AOH$  for the  
 173 **warmthawed**-bedded areas, i.e.  $T_{bm} = T_{melt}$ , because observed surface ice speed errors  
 174 are proportionally much less in **warmthawed**-bedded areas (corresponding to fast flow  
 175 regions) than in **coldfrozen**-bedded area (correspond to slow flow regions).

176 To mitigate the impact of substantial differences in observed surface ice speed  
 177 across various areas, we also define "relative overheating" ( $ROH$ ) and "relative  
 178 overcooling" ( $ROC$ ), dividing  $AOH$  and  $AOC$  by the observed surface ice speed  
 179 respectively:

$$180 \quad ROH = \frac{\max(0, U_{sm} - U_{obs})}{U_{obs}}, \quad (3)$$

$$181 \quad ROC = (T_{melt} - T_{bm}) \times \frac{U_{bm}}{U_{obs}}. \quad (4)$$

182 Overheating and overcooling inconsistencies are calculated on **warmthawed** bed  
 183 and **coldfrozen** bed, respectively. To evaluate the inconsistencies for the whole domain,  
 184 we linearly normalized the overheating inconsistency and overcooling inconsistency to  
 185 range from 0 to 1 and then sum them as:

$$186 \quad ACI = L_N(AOC) + L_N(AOH), \quad (5)$$

$$187 \quad RCI = L_N(ROC) + L_N(ROH), \quad (6)$$

188 where  $ACI$  means absolute combined inconsistency,  $RCI$  represents relative combined  
 189 inconsistency, and  $L_N$  represents linear normalization. Taking  $AOC$  as an example, its  
 190 linear normalization is:

$$191 \quad L_N(AOC) = \frac{AOC - AOC_{min}}{AOC_{max} - AOC_{min}}. \quad (7)$$

192 Therefore, we obtain 6 metrics consisting of three absolute inconsistencies (*AOH*, *AOC*,  
193 *ACI*) and three relative inconsistencies (*ROH*, *ROC*, *RCI*).

194 These 6 indicators can comprehensively analyze the temperature-sliding  
195 inconsistency in the inversion results of ice sheet model. For each metric, we rank the  
196 eight GHF datasets from 1 (least inconsistent) to 8 (most inconsistent). The final score  
197 for each dataset is the average of its ranks across the six metrics to ensure a  
198 comprehensive evaluation, as a reasonable simulation result should perform well across  
199 ~~warm~~thawed bed, ~~cold~~frozen bed, and the whole region. We only consider grounded  
200 ice and exclude points located at the domain boundary due to relatively poor model  
201 performance there.

202 The specific metrics that we use to quantify this inconsistency could be  
203 adaptable~~changed~~, for example by using a squared error term instead of the linear error  
204 terms that we used. However, the general practice of ~~emphasizing~~earing about and  
205 quantifying the inconsistency between a sliding inversion and the temperature/rheology  
206 field used as an input to that inversion is novel~~is new~~.

## 207 **2.2 Methodology in Huang et al. (2024)**

208 Huang et al. (2024) employed thermo-mechanical coupled simulations using eight  
209 GHF datasets to investigate the steady-state thermal regime of Totten Glacier. The  
210 methodology ~~comprised~~ involved two interconnected modeling components:

- 212 1. Forward Modeling: An enhanced shallow-ice approximation model integrated with  
213 a subglacial hydrology module was utilized to simulate englacial temperature profiles.
- 214 2. Inverse Problem: A full-Stokes ice flow model was applied to resolve basal friction  
215 coefficients through inverse analysis, to minimize the misfit between simulated and  
216 observed velocities while simultaneously generating velocity predictions.

217 A feedback loop was then established: the velocity outputs from the inverse model  
218 were used to refine key parameters in the forward model - specifically constraining the  
219 basal slip ratio, rheological properties, and shape functions. This bidirectional coupling  
220 process underwent multiple iterations to achieve convergent steady-state solutions.

221 Huang et al. (2024) utilized~~used~~ some radar specularly content data to  
222 differentiate localized wet (thawed) versus dry (frozen) basal conditions and used this  
223 data as a two-sided constraint on the basal thermal state. They compared modeled basal  
224 thermal states ~~derived from~~ with different GHFs to evaluate the reliability of the GHF  
225 datasets.

## 226 **2.3 Distinction from Huang et al. (2024)**

227 In Huang et al. (2024), modelled surface velocity velocities are compared with  
228 observations over the whole domain during the inversion for basal parameters for each  
229 GHF dataset. ~~is compared with the observed over the whole domain in the inversion for~~

231 ~~basal parameters for each GHF data. Here, surface velocities act as the observational~~  
232 ~~constraints for the mechanical inversion. The observational constraints for a mechanical~~  
233 ~~inversion are surface velocities.~~

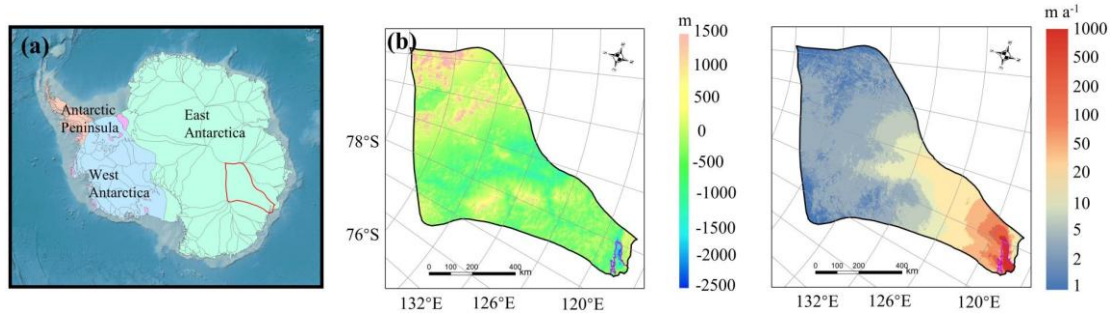
234 ~~Although the overheating metrics here use the surface velocities and can thus be~~  
235 ~~considered thought of as a subset of the inversion residual, our overcooling metrics are~~  
236 ~~based on the basal sliding velocity derived from the inversion, which does not part of~~  
237 ~~enter into the residual of a mechanical inversion's residual. A mechanical inversion does~~  
238 ~~not take into account the physical plausibility of the sliding result it produces. Therefore,~~  
239 ~~it is not circular reasoning to compare two different parts of a model to each other;~~  
240 ~~rather, it is a check of internal consistency, or lack thereof. A mechanical inversion may~~  
241 ~~be able to fit the surface velocity observations equally well when forced with many~~  
242 ~~different models of the ice sheet thermal structure and rheology; however, if some of~~  
243 ~~those models require high sliding velocities in frozen-based regions, then they should~~  
244 ~~be downweighted in comparison to models that show a good agreement between basal~~  
245 ~~temperature and velocity.~~

246 ~~The method here does not require any additional observations beyond the surface~~  
247 ~~velocities used in the mechanical inversion. However, there are “independent~~  
248 ~~constraints” in the method here, which are not observations, but rather the a priori~~  
249 ~~physical understandings that: 1) rapid sliding requires warm basal temperatures and~~  
250 ~~subglacial water; 2) reducing the basal slip coefficient cannot prevent the ice from~~  
251 ~~flowing by internal shear deformation. The inconsistency metrics developed in this~~  
252 ~~paper are an attempt to quantify and rank the extent to which these basic (and~~  
253 ~~uncontroversial) physical understandings are violated.~~

### 255 **3. Application to Totten Glacier with Different GHFs**

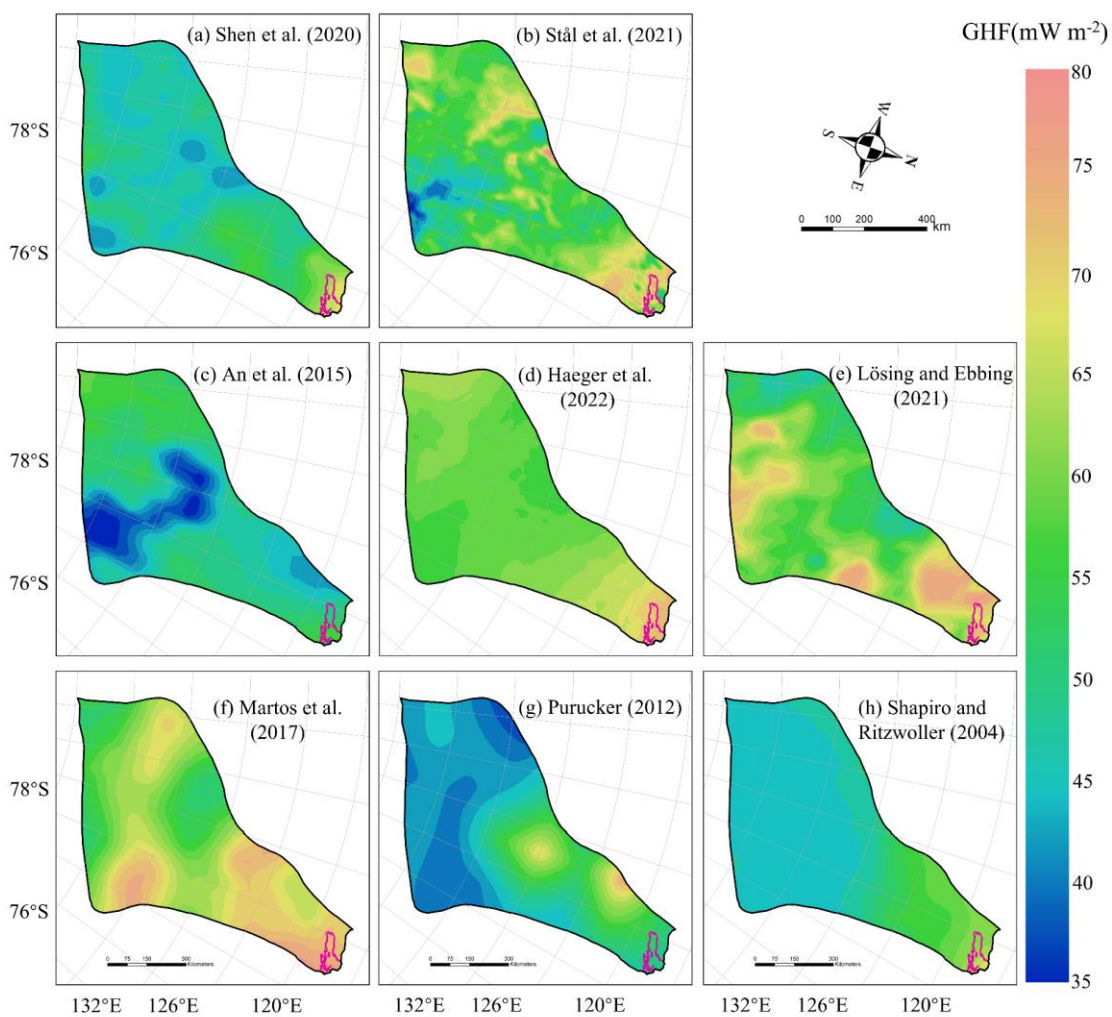
#### 256 **3.1 Study domain and Data**

257 We apply our method to evaluate simulated ice temperature and ice velocity in  
258 Totten Glacier ~~with eight GHF datasets~~ by ~~following~~ Huang et al. (2024) ~~and using~~  
259 ~~eight GHF datasets~~. Huang et al. (2024) used the present-day surface ice temperature  
260 (Le Brocq et al., 2010), ~~observed surface velocity from MEaSURES InSAR-Based~~  
261 ~~Antarctic Ice Velocity Map, version 2 (Rignot et al., 2017)~~ and ice sheet topography  
262 data from BedMachine Antarctica, version 2 (Morlighem et al., 2020). The eight GHF  
263 datasets were derived by various methodologies, resulting in significant differences in  
264 both spatial distribution and magnitude (Fig. 2). GHF fields from Stål et al. (2021),  
265 Haeger et al. (2022), Lösing and Ebbing (2021) and Martos et al. (2017) generally  
266 exhibit higher magnitudes than the other GHFs.



267

268 **Figure 1.** (a) Geographic location of Totten Glacier (red outline) in Antarctica; (b) bed  
 269 elevation of Totten Glacier, the purple curve represents the grounding line; (c) observed  
 270 surface velocity.  
 271



272

273 **Figure 2.** The spatial distribution of the 8 GHF datasets for Totten Glacier (a–h) used  
 274 as input data in Huang et al. (2024). The purple line depicts the grounding line.

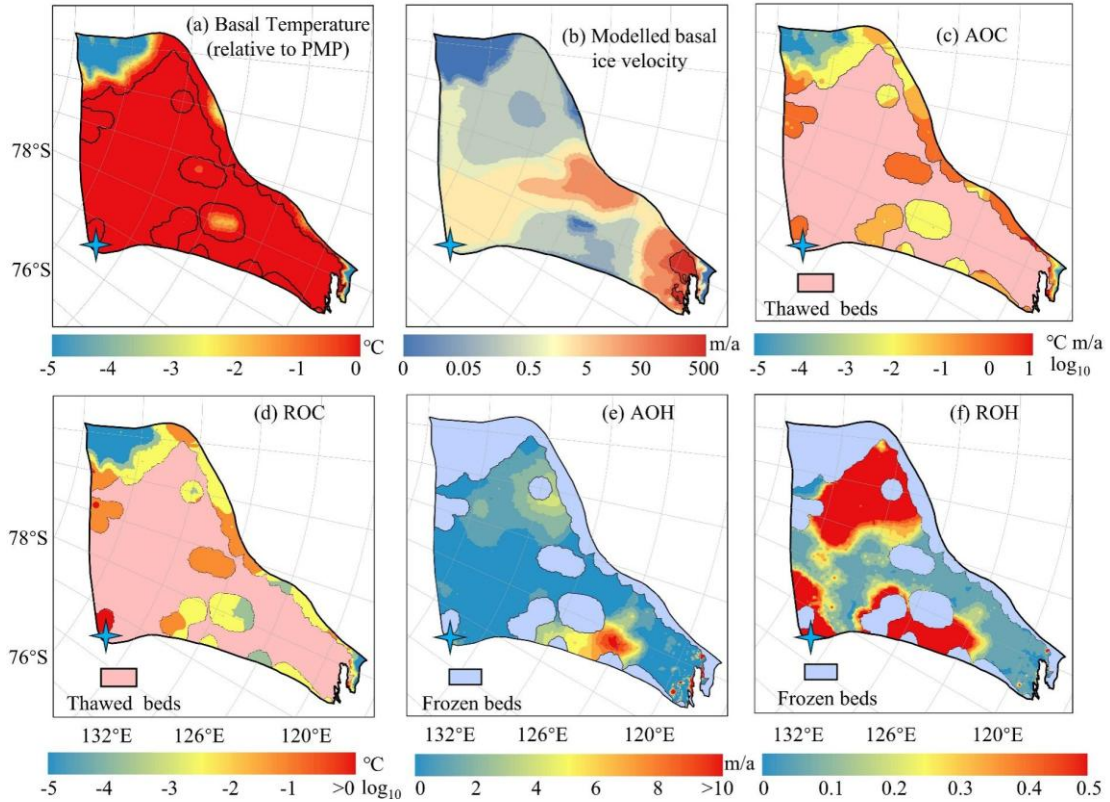


275  
276  
277  
278  
279  
280  
281  
282  
283  
284  
285  
286  
287  
288  
289  
290  
291  
292  
293  
294  
295  
296  
297  
298

The spatial distribution of modelled basal temperature using the 8 GHFs displays both similarities and heterogeneity. In the northern part of Totten Glacier, there is a consistent warmthawed-bedded pattern across all eight simulation results (Fig. S1), which originates from the grounding line and extends upstream to approximately 71°S. This warmthawed-bedded area is not contiguous with the lateral boundaries of Totten Glacier but is instead bordered by coldfrozen bed. All 8 GHF datasets produce low basal ice temperatures in the inland southwest, with Purucker et al. (2012), Shapiro and Ritzwoller (2004), Shen et al. (2020) and Lösing and Ebbing (2021) being colder. The basal ice velocities modelled from the 8 different GHF datasets produce similar spatial distributions (Fig. S2), which can be expected as they were derived using the same inverse method and constrained by the identical observed surface ice velocity. The modelled basal ice velocity is fast near the grounding line and its upstream area. There are also high velocities between 70°S and 72°S close to the western boundary of Totten Glacier, which are associated with subglacial canyon features in the basal topography (Fig. 1b) and observed fast surface ice velocity there.

### 3.2 Spatial Distribution of Inconsistencies with one GHF dataset

In this section, we show the spatial fields of the inconsistencies metrics (Section 2.1) for the modelled result in Huang et al. (2024), usingwith Martos et al. (2017) GHF as an example. This example illustrates the interpretation process before conducting a comprehensive comparative analysis for the result with 8 GHF datasets.



299

300 Figure 3. Spatial distribution of modelled basal ice temperature (a), modelled basal ice  
 301 speed (b), AOC (c), ROC (d) inconsistencies in modelled cold frozen-bedded regions,  
 302 and AOH (e) and ROH (f) inconsistencies in modelled warm thawed-bedded regions  
 303 associated with Martos et al. (2017) GHF. The colormap in (c) and (d) is on logarithmic  
 304 scale. The pink region in (c) and (d) represents modelled thawed bed, while the blue  
 305 region in (e) and (f) indicates frozen-bedded areas.

306

307 The modelled result based on the Martos et al. (2017) GHF reveals extensive  
 308 regions of thawed bed with limited areas of frozen bed. The frozen bed is predominantly  
 309 located in the southern corner of the study domain, where the modelled basal ice speed  
 310 approaches zero, consistent with cold basal ice temperature. Consequently, the AOC  
 311 inconsistency at this marginal zone is negligible (Fig. 3). Along the western margin of  
 312 Totten Glacier, basal ice temperature remains below the pressure melting point, albeit  
 313 approaching it. However, localized regions exhibit high basal velocities of several tens  
 314 of meters per year, contradicting the presence of a frozen bed and resulting in large  
 315 AOC inconsistencies.

316 Conversely On the other hand, large AOH values are observed between 69°S and 71°S  
 317 in the eastern Totten Glacier region, where the simulated surface ice speed exceeds  
 318 observational data by  $>5 \text{ m a}^{-1}$  (Fig. 3e). In this area, the modelled basal ice temperature

319 reaches the pressure melting point, with the modelled basal ice speed at approximately  
320  $0.05 \text{ m a}^{-1}$ . Basal friction inversion failed to reproduce observed surface ice speed due  
321 to the model's overestimation of ice temperature and softness. This pronounced velocity  
322 mismatch highlights a fundamental inconsistency in the eastern glacier region, likely  
323 originating from discrepancies in the input datasets. Regions of high ROH and ROC  
324 values coincide with areas of relatively high AOH and AROC, particularly where the  
325 observed surface velocities are slow, as per their formulations.

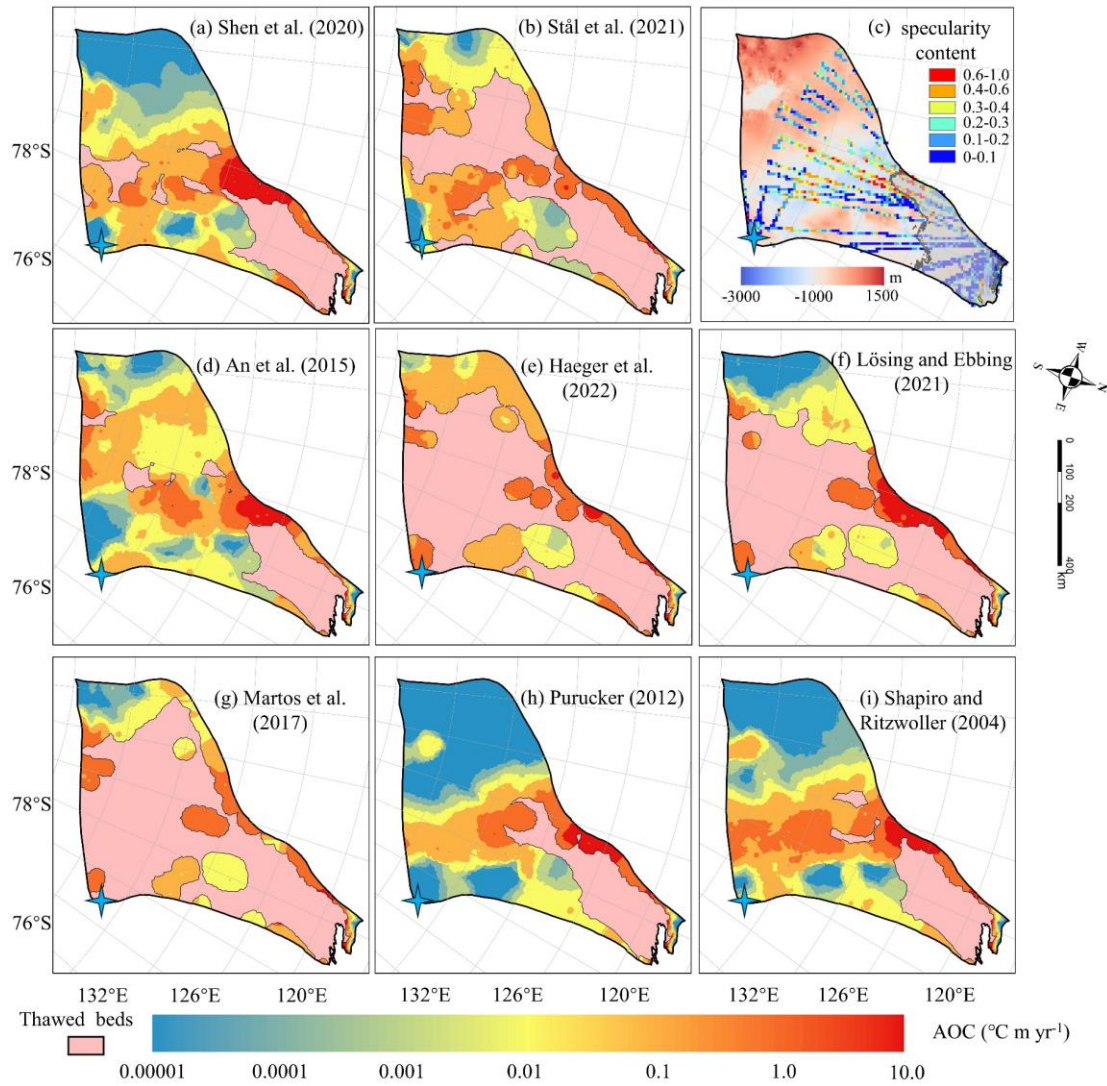
### 3.23.3 Spatial Distribution of Inconsistencies with eight GHF datasets

326  
327 We calculate the absolute inconsistencies, *AOH*, in the ~~warmthawed~~ bed, and *AOC*  
328 in the ~~oldfrozen~~ bed. The spatial distribution of *AOC* reveals that most GHF datasets  
329 exhibit significant local overcooling inconsistencies at the subglacial canyon between  
330  $70^\circ\text{S}$  and  $72^\circ\text{S}$  (Fig. 34). There is fast basal sliding in the inverse model results (Fig.  
331 S2), however, the modelled basal ice temperatures inferred from most of the GHF  
332 datasets are below the pressure melting point (Fig. S1). High specular content in  
333 radar data (Fig. 34c) suggests the presence of basal water in the subglacial canyons here  
334 (Dow et al., 2020; Huang et al., 2024), which also suggests that the basal ice  
335 temperature should be at the pressure melting point and confirms the inconsistency  
336 between the modelled temperature and velocity fields.

337  
338 The area near the grounding line is characterized by fast ice flow and ~~warmthawed~~  
339 bed (Fig. 34), yet some of the margin is ~~oldfrozen~~-bedded with modelled basal  
340 temperature below the pressure melting point, resulting in high *AOC*. Overall, modelled  
341 results with most GHF datasets show small overcooling inconsistencies. The modelled  
342 results using GHF from Purucker et al. (2012), Shapiro and Ritzwoller (2004), Shen et  
343 al. (2020), Lösing and Ebbing (2021) exhibit no overcooling inconsistency in  
344 southwestern Totten Glacier (Fig. 34).

345 The spatial distribution of relative overcooling inconsistencies, *ROC* (Fig. 54),  
346 differs from that of absolute inconsistencies, *AOC*, and is due to the spatial variability  
347 in surface ice speed. The largest value of *ROC* across most GHF occurs at Dome C,  
348 where the observed surface ice speed is close to zero.

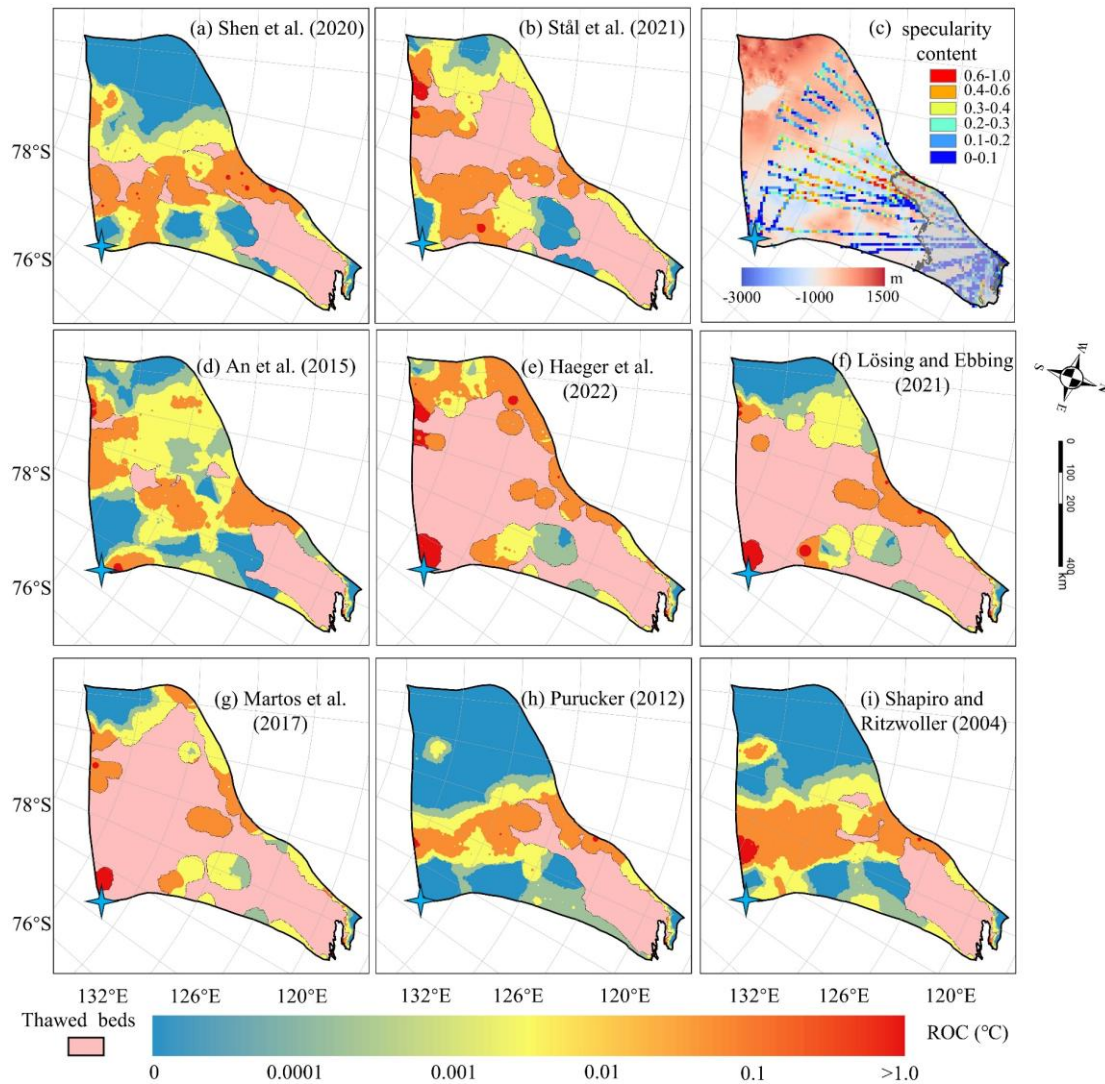
349



350

351 **Figure 34.** Spatial distribution of *AOC* inconsistency in modelled ~~cold~~frozen-bedded  
 352 regions (**a-b, d-i**) associated with the GHFs (**a-h**) in Fig. 2. The colormap is on  
 353 logarithmic scale. The pink region represents modelled ~~warm~~thawed bed. (**c**)  
 354 Specularity content sourced from radar data collected by ICECAP (Dow et al., 2020)  
 355 with the bed elevation in the background. Gray area in (**c**) corresponds to surface speed  
 356 exceeding 30 m yr<sup>-1</sup>. The blue star represents Dome C.

357



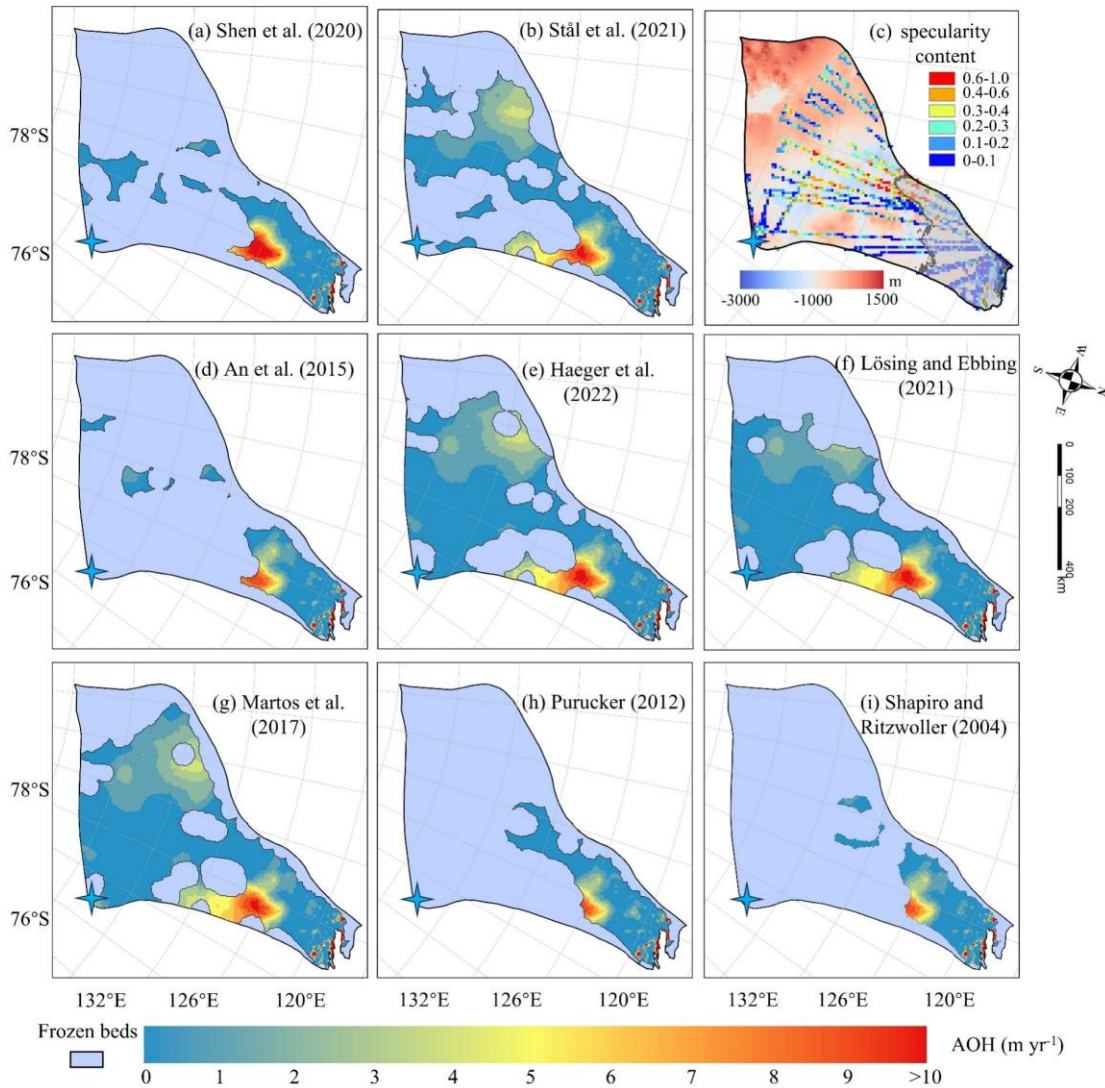
358  
 359  
 360  
 361  
 362  
 363  
 364  
 365

Figure 54. The spatial distribution of relative overcooling (ROC) inconsistency in cool beds with (a), (b) and (d) to (i) corresponding to the GHFs (a – h) in Figure 2. The pink area represents the **warmthawed** beds. Dome C is marked by a blue star. (c) Locations of specular content derived from radar data collected by ICECAP (Dow et al., 2020) and with the bed elevation in the background. The gray curve is the contour of the surface speed of  $30 \text{ m yr}^{-1}$ . Note the colormap is non-linear.

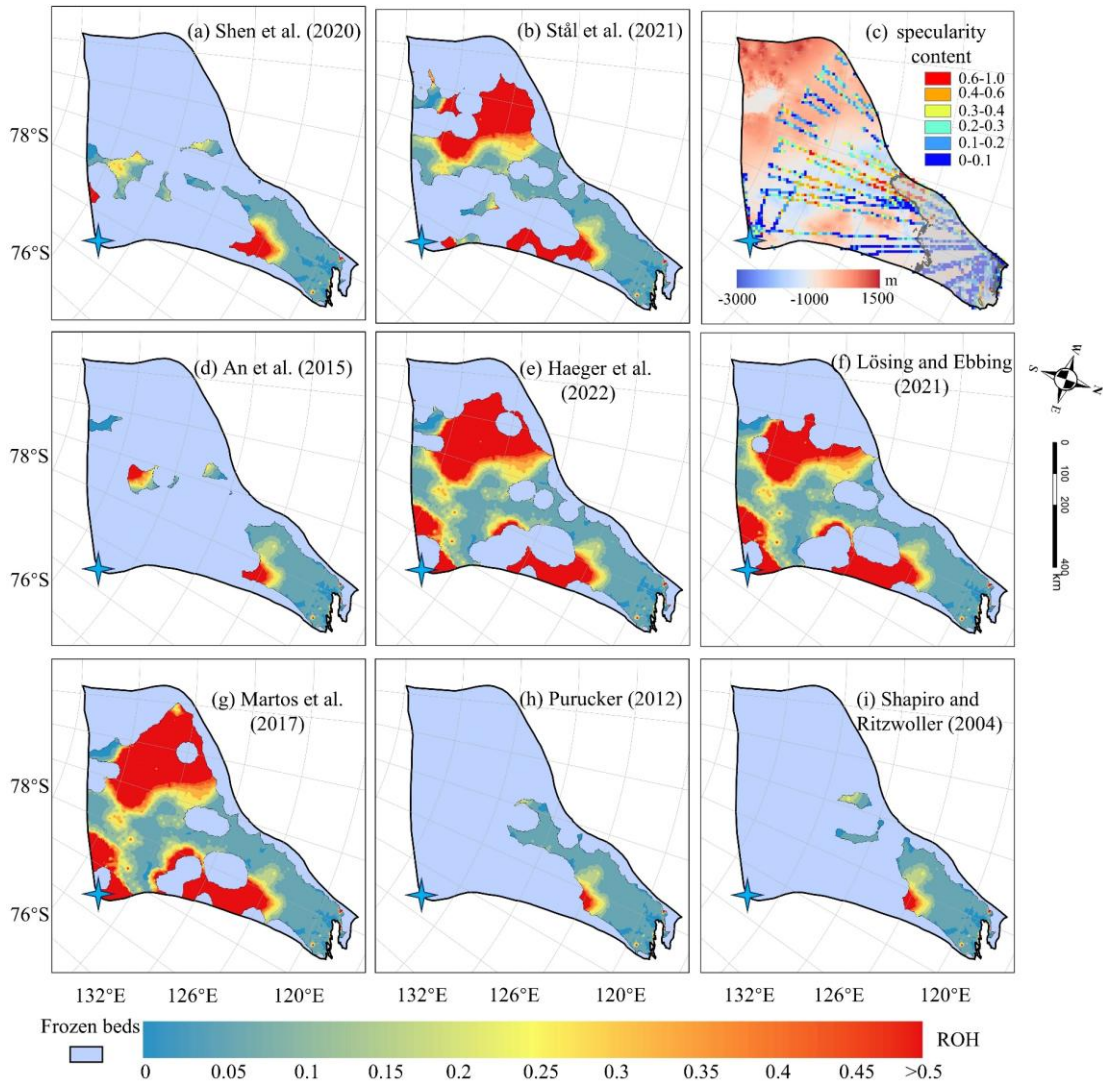
366  
 367  
 368  
 369  
 370  
 371

The GHF datasets of Stål et al. (2021), Haeger et al. (2022), Lösing and Ebbing (2021) and Martos et al. (2017) which have higher than average GHF values provide larger areas of **warmthawed** bed than the other 4 GHFs. The simulations with all 8 GHFs yield similar spatial distributions of *AOH* (Fig. 65) on the common area of **warmthawed** bed, and similar locations of high *AOH* values. A common high *AOH* area is located between  $69^\circ\text{S}$  and  $72^\circ\text{S}$  in the eastern part of Totten Glacier, due to simulated surface

372 ice velocities greatly exceeding the observed surface ice velocities. Low specularity  
 373 content from radar data (Fig. 65c) suggests there is no basal water in the area (Dow et  
 374 al., 2020; Huang et al., 2024). Therefore, it is likely that the basal ice temperature is  
 375 overestimated there. The simulations with all the 8 GHFs also yield similar spatial  
 376 distribution of *ROH* (Fig. 76), but its largest values are mostly in the slow flowing  
 377 region as one may expect from its formulation (Eq. (3)).



378  
 379 **Figure 65.** Spatial distribution of *AOH* in warmthawed-bedded regions with (a-b, d-i)  
 380 corresponding to the GHFs (a-h) in Fig. 2. The blue region indicates coldfrozen-bedded  
 381 areas. (c) Locations of specularity content, same as Fig. 34c. The blue star represents  
 382 Dome C.  
 383



384  
 385 Figure 76. The spatial distribution of relative overheating (ROH) inconsistency in  
 386 ~~warmthawed~~ beds with (a), (b) and (d) to (i) corresponding to the GHFs (a - h) in Figure  
 387 2. The light purple mask represents the ~~old~~ frozen beds. (c) Locations of specularity  
 388 content (coloured points), same as Fig. 65.

389

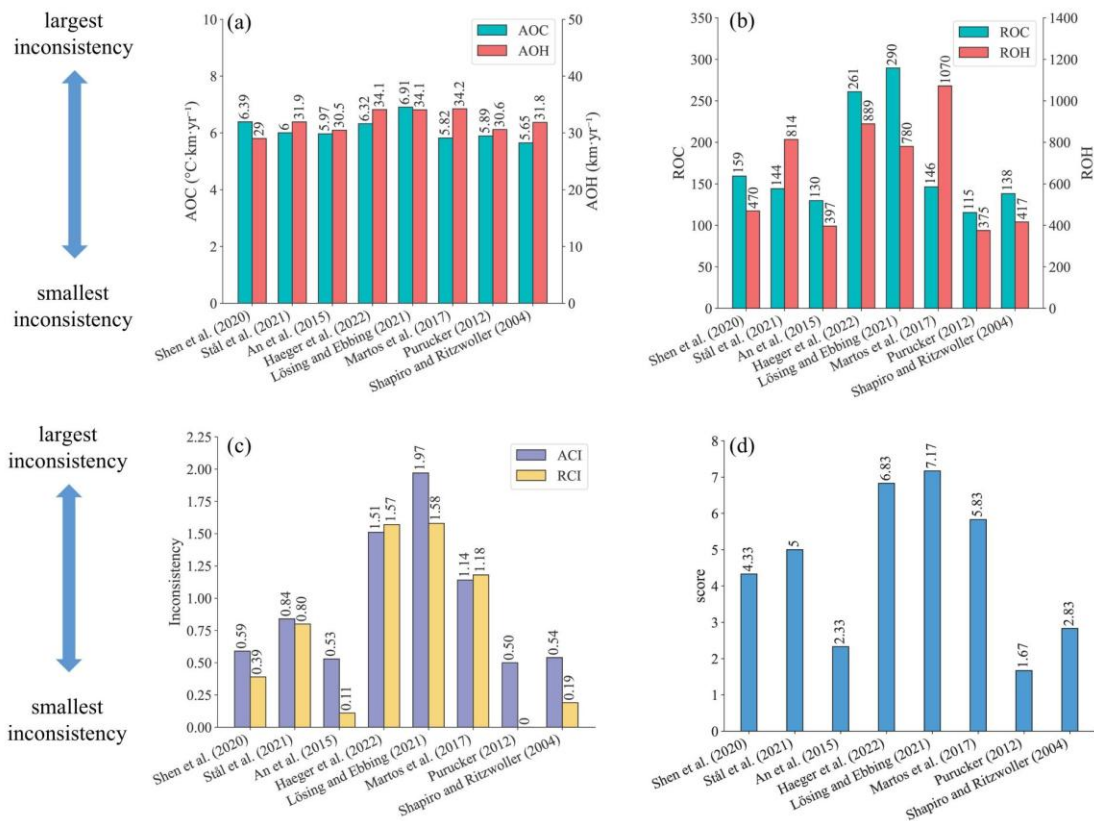
### 390 3.33.4 Evaluation of Model Inconsistency with Eight GHFs

391 To assess the overall inconsistency of each geothermal heat flux dataset, we  
 392 calculate the sum of each metric over all points. All inconsistency indices for the  
 393 simulation results using the eight GHF datasets are illustrated in Fig. 87. The  
 394 overheating inconsistency associated with Purucker et al. (2012) and Shapiro and  
 395 Ritzwoller (2004) GHFs is predominantly localized in fast-flowing regions.  
 396 Consequently, after normalization by the surface observed ice speed, their relative  
 397 rankings improve (Fig. 87). The GHFs from Purucker et al. (2012), An et al. (2015),

398 Shapiro and Ritzwoller (2004), and Shen et al. (2020) demonstrate balanced  
399 performance with respect to both overheating and overcooling inconsistency metrics,  
400 thereby securing the top four positions in both *ACI* and *RCI*. Their *ACI* values exhibit  
401 similarity, ranging from 0.50 to 0.59 (Fig. 87c). In contrast, simulation result utilizing  
402 Martos et al. (2017) GHF exhibits low *AOC* but high *AOH*. Simulation results utilizing  
403 Stål et al. (2021) GHF show low *ROC* but relatively high *ROH*. Notably, simulation  
404 results employing GHFs from Martos et al. (2017), Haeger et al. (2022), and Lösing  
405 and Ebbing (2021) demonstrate comparably high *AOH* values. These four GHF  
406 datasets—Martos et al. (2017), Stål et al. (2021), Haeger et al. (2022), and Lösing and  
407 Ebbing (2021)—are ranked in the bottom four positions for both *ACI* and *RCI* metrics.  
408 Furthermore, the ranking order of the eight GHFs remains consistent between *ACI* and  
409 *RCI*.

410 The final averaged ranking (Fig. 87d) across the indices is also the same as that of  
411 *ACI* and *RCI*. Purucker et al. (2012), An et al. (2015) and Shapiro and Ritzwoller (2004)  
412 GHFs occupy the top three positions. Following closely, Shen et al. (2020) and Stål et  
413 al. (2021) GHFs secure the 4th and 5th positions, respectively. Martos et al. (2017),  
414 Haeger et al. (2022) and Lösing and Ebbing (2021) GHFs are ranked as the bottom  
415 three among the eight GHFs in Totten Glacier. The thermal state produced by the  
416 optimal GHF result shows that warmthawed beds predominantly cluster around the  
417 grounding line and its upstream regions. Conversely, the inland areas of Totten largely  
418 exhibit cold temperatures, with relatively sparse warmthawed-bedded areas.





419

420 **Figure 87.** Six inconsistency indicators and the final ranking of 8 GHF datasets. **(a)** the  
 421 absolute overcooling and overheating inconsistencies, *AOC* and *AOH*; **(b)** the relative  
 422 overcooling and overheating inconsistencies, *ROC* and *ROH*; **(c)** the absolute and  
 423 relative combined inconsistencies, *ACI* and *RCI*; **(d)** the average of ranking scores from  
 424 1 to 8 using the six inconsistency indicators. The value of inconsistencies and scores  
 425 are labeled at the top of the bars.

426

## 427 4. Discussion

### 428 4.1 Causes of Inconsistencies and Sources of Uncertainty

429 Our method evaluates the quality of an ice sheet temperature field by quantifying  
 430 the inconsistency between that temperature field and the velocity field that is obtained  
 431 if that temperature field is used to compute the rheology in a mechanical inversion.  
 432 Because mechanical inversions use surface velocity observations as a constraint, we  
 433 have developed an indirect method for using surface velocity observations to check the  
 434 quality of an englacial temperature simulation. However, the mere fact that  
 435 inconsistencies exist does not by itself tell us what caused those inconsistencies.

436 Broadly speaking, the measured inconsistencies can come from two sources:  
 437 temperature or velocity. Uncertainties in any of the input datasets used to compute those  
 438 two fields can produce inconsistencies, as can simplifications in the model physics.

439 Here, we have tested the influence of one particular boundary condition, GHF, since  
440 that field is particularly hard to constrain. Because all other inputs are kept constant,  
441 the differences in the inconsistencies that we calculated between different simulations  
442 can be attributed to the GHF fields. However, we also found that all of the models we  
443 tested had non-zero inconsistency (Fig. 34; Fig. 65). The absolute inconsistencies, *AOH*  
444 and *AOC*, had particularly small between-model variability in comparison to their mean  
445 value. This could be because none of the input GHF fields correctly captured the true  
446 GHF, but it could also indicate problems with other model inputs. For instance, the  
447 surface temperature used in Huang et al. (2024) represents the present-day climate, but  
448 the thermal structure of the ice sheet may reflect colder temperatures during the last  
449 glacial cycle. We discuss an additional experiment we performed to test the influence  
450 of uncertainty in surface temperature on our inconsistency metrics in Section 4.3 below.  
451 By contrast, surface accumulation rate should have been lower during glacial periods,  
452 which would have a warming influence on ice sheet temperatures. Uncertainties in bed  
453 topography should influence both our thermal and our mechanical models, with deeper  
454 ice being more likely to be warm, and with errors in ice thickness producing  
455 compensating errors in basal sliding in our mechanical inversion. In the study of Huang  
456 et al. (2024), BedMachine v2 was used for ice thickness and subglacial topography.  
457 However, Bedmap3 (Pritchard et al., 2025) has better-resolved mountains and smoother  
458 trough margins.

459 The simulation results we use from Huang et al. (2024) came from a 3D isotropic  
460 full-Stokes ice flow model. While full-Stokes is generally considered the gold standard  
461 of ice sheet mechanical modeling, the use of an isotropic rheology may not be valid in  
462 some parts of the ice sheet, such as near ice divides or at the margin of an ice stream  
463 where the history of past ice deformation creates anisotropic crystal fabric that affects  
464 the present-day mechanical properties (Martín et al., 2009; Zhao et al., 2018b; Zwinger  
465 et al., 2014). Isotropic flow laws often require the use of an “enhancement factor” for  
466 vertical shear in the lower part of the ice column, an ad hoc correction that would have  
467 a particularly large influence on our computed overcooling metrics. Thus the isotropic  
468 flow law potentially introduces errors in modelled strain rates and, hence, bias in basal  
469 sliding velocities obtained by inversion methods (Budd and Jacka, 1989; Gerber et al.,  
470 2023; Rathmann and Lilien, 2022). Simulated surface ice velocities can be influenced  
471 by other factors in addition to ice fabric; shear margins are also impacted by  
472 accumulated rupture, such as damage along a shear margin (e.g., Benn et al., 2022;  
473 Lhermitte et al., 2020; Schoof, 2004; Sun et al., 2017). Ice deposited during the last  
474 glaciation has different chemistry (especially concentrations of chloride and possibly  
475 sulphate ions) which leads to smaller crystals that develop a strong, near-vertical,  
476 single-maximum fabric (Paterson, 1991). However, ice fabric data is sparse, known  
477 from direct observations at ice cores (Azuma and Higashi, 1985) or inferred from

478 specialized radar measurements (Fujita and Mae, 1994; Jordan et al., 2022), and its  
479 impact beyond the scope of this study as we refrain from incorporating additional  
480 observational data relying only on widely-available surface ice velocities.

481 Our inconsistency metrics are designed to provide bidirectional constraints,  
482 wherein the model is penalized for both overheating and overcooling. By adopting this  
483 bidirectional constraint framework, we aim to mitigate the risk of unidirectional  
484 constraints leading to excessively cold or warm outcomes being deemed optimal.  
485 However, our inconsistency metrics only provide a bidirectional constraint when  
486 viewed in a spatially integrated sense. Locally, we only have unidirectional constraints.  
487 This is because our overheating metrics are only computed where the bed is at the  
488 melting point, and our overcooling metrics are only computed where the bed is below  
489 the melting point. This makes methodological sense, as we know for sure that sliding  
490 must only occur where the bed is **warmthawed**. However, in reality it is entirely possible  
491 that some of the areas where the modelled bed reaches the pressure melting point are  
492 still too cold (the modelled melt rate is lower than the real melt rate), and conversely, it  
493 is also possible that some of the areas where the modelled bed is below the pressure  
494 melting point are still too warm (the real temperature is colder still). Our method cannot  
495 identify these areas. Thus, our inconsistency metrics may underestimate variability in  
496 the ice sheet thermal state: we have no way to penalize **coldfrozen** regions that are not  
497 cold enough or **warmthawed** regions that are not warm enough. We leave the  
498 development of these constraints to future work.

499

## 500 4.2 Sensitivity of Inconsistencies to GHF Datasets

501 Comparing the GHF dataset rankings between this study and Huang et al. (2024),  
502 we find that the top 4 and the bottom 4 are the same in the two studies, albeit with slight  
503 variations in ranking. The lower ranking of Shen et al. (2020) in this study may be  
504 attributed to several factors. Firstly, Huang et al. (2024) excludes areas with ice speed  
505 exceeding  $30 \text{ m a}^{-1}$  (Fig. 34c) because specular content is an ambiguous indicator of  
506 wet beds there. Secondly, the GHF from Shen et al. (2020) yields higher basal  
507 temperature and also faster basal ice velocities in most of the **coldfrozen** bed of Totten  
508 Glacier, hence exhibits greater overcooling inconsistency, compared with Purucker et  
509 al. (2012), leading to a decrease in its rankings (Fig. S3). Lastly, Huang et al. (2024)  
510 primarily relied on specular content, while our study evaluated datasets based on  
511 inconsistencies in the simulation results. Despite these methodological differences, both  
512 studies identified four relatively well-performing GHF datasets for Totten Glacier,  
513 which exhibit similar distributions of **warmthawed** and **coldfrozen** beds when compared  
514 to the other four datasets (Fig. 34 and Fig. 65). This similarity underscores that the  
515 **warmthawed** bed is concentrated near and upstream of the grounding line. Datasets

516 from Stål et al. (2021), Martos et al. (2017), Haeger et al. (2022), and Lösing and Ebbing  
517 (2021) exhibit a tendency to overestimate GHF in central Totten Glacier.

518 Simulations employing GHF datasets from Stål et al. (2021), Martos et al. (2017),  
519 Haeger et al. (2022), and Lösing and Ebbing (2021) yield more extensive ~~warmthawed~~-  
520 bedded regions and are expected to exhibit greater overheating inconsistency.  
521 Nevertheless, these models also exhibit relatively high overcooling inconsistency  
522 despite the limited extent of ~~coldfrozen~~-bedded regions. We quantified the  
523 discrepancies between these four GHF datasets and the Purucker et al. (2012) GHF in  
524 terms of modelled basal velocity, basal temperature relative to the pressure melting  
525 point, and *AOC* (Fig. S5). The Purucker et al. (2012) GHF yields lower basal ice  
526 temperatures and slower basal velocities across most ~~coldfrozen~~-bedded regions,  
527 consequently resulting in lower *AOC* values compared to the other four GHF datasets.

528

### 529 4.3 Implications for Ice Sheet Dynamics

530 While evaluating inconsistencies highlights the spatial distribution of mismatches,  
531 it does not inherently elucidate their underlying causes. Evaluating the inconsistencies  
532 reveals where mismatches occur but not why they arise. The primary factors to  
533 investigate are surface temperature, GHF, accumulation rate, and ice thickness,  
534 representing the most critical boundary conditions. Furthermore, integrating multiple  
535 sources of prior knowledge can help constrain model parameters:

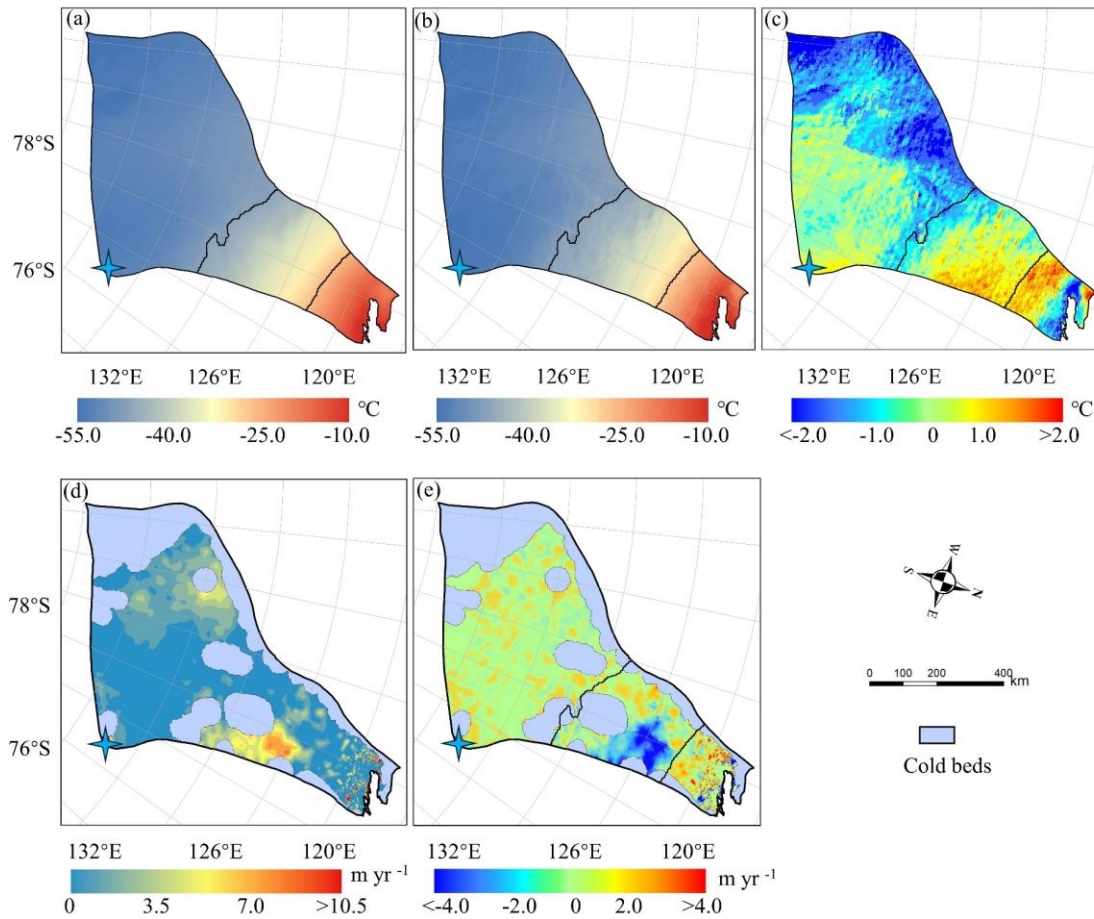
536 1. High-resolution radar measurements: The availability of ice thickness data along  
537 flight lines should be assessed to validate geometric boundary conditions. Check  
538 availability of ice thickness data along flight lines to validate geometric boundary  
539 conditions.

540 2. Paleoclimate context: Historical climate reconstructions indicate significantly colder  
541 surface temperatures during glacial periods compared to present-day conditions, with  
542 correspondingly lower accumulation rates. These paleo-temperature conditions likely  
543 induced a long-term thermal memory within the ice column, potentially contributing to  
544 observed discrepancies between modeled and measured basal properties.

545 Therefore, we recommend a systematic evaluation of: (1) The spatial distribution  
546 of radar-derived ice thickness measurements; (2) The temporal consistency of surface  
547 temperature boundary conditions; (3) The sensitivity of model results to GHF variations;  
548 (4) Accumulation rate reconstructions during key climatic periods. This multi-faceted  
549 approach helps isolate the causes of inconsistencies in ice sheet simulations.

550 There is a common area between 69°S and 72°S in the eastern part of Totten  
551 Glacier with the largest *AOH* (Fig. 6) for all the GHFs varying from 48 to 70 mW m<sup>-2</sup>,  
552 which suggests that the *AOH* inconsistency is from other ice sheet properties rather than  
553 GHF. Zhang et al. (2022) reconstructed Antarctic near-surface air temperature based on  
554 MODIS land surface temperature measurements and in situ air temperature records

555 from meteorological stations from 2001 to 2018. We compared the reconstruction of  
 556 near-surface air temperature in the year 2001 (Zhang et al., 2022) and the ALBMAP v1  
 557 dataset used in Huang et al. (2024). The surface air temperature in the area with large  
 558 *AOH* from ALBMAP v1 is 0.6-3.1 °C higher than that from the reconstructed near-  
 559 surface air temperature in 2001 (Fig. 98). The MODIS-based near-surface air  
 560 temperature product shows warming in Totten Glacier from 2001 to 2018. Even so, the  
 561 surface air temperature in the area with large *AOH* from ALBMAP v1 is still higher  
 562 than that in 2018 but over a smaller area. Therefore, we infer that the large *AOH* may  
 563 be attributed to the present-day ice surface temperature derived from ALBMAP v1 in  
 564 this area being unrealistically warm. The englacial temperature will be lower than  
 565 present-day ice sheet surface temperature used in the model but warmer than the  
 566 average surface temperature during the last glacial-interglacial cycle. We lowered the  
 567 surface ice temperature in this area by 1 °C, reran the simulation, and found that *AOH*  
 568 with all the GHFs was halved (Fig. 98e).  
 569



570

571 **Figure 89.** Surface ice temperature from ALBMAP v1 (a) and MODIS-based near-  
572 surface air temperature (b) in the year 2001, and their difference (c). (d) The AOH using  
573 modified surface ice temperature by reducing the temperature between the two thick  
574 black curves (contour lines of  $-44\text{ }^{\circ}\text{C}$  and  $-26\text{ }^{\circ}\text{C}$ ) in (a) by  $1\text{ }^{\circ}\text{C}$  and GHF of Martos  
575 et al. (2017). (e) The difference between the AOH using cooler surface ice temperature  
576 and the original AOH. The blue star represents Dome C.

577  
578 Given that data assimilation and inverse methods are widely employed to infer  
579 basal friction coefficients in ice sheet simulations, it is essential to acknowledge the  
580 impact of the inconsistencies identified in our study on ice sheet dynamics. A ~~cold~~frozen  
581 bed is supposed to provide substantial resistance and limit basal sliding; however, if the  
582 basal temperature is overestimated, it may decrease viscosity and enhance basal sliding.  
583 This overheating inconsistency would lead to an overestimation of ice flow speeds,  
584 discharge, and the dynamic ice loss (Artemieva, 2022; Burton-Johnson et al., 2020).  
585 Similarly, under representation of ~~warm~~thawed bedding would slow ice discharge  
586 estimates, and hence potential ice sheet response to climate warming. The basal thermal  
587 regime critically influences the stability of grounding lines and the behavior of ice  
588 streams. In a warming climate, increases in geothermal or frictional heating can trigger  
589 basal thawing in these areas, lowering basal friction and potentially initiating rapid  
590 grounding line retreat—a key component of marine ice sheet instability (MISI) (Reese  
591 et al., 2023; Ross et al., 2012). Without incorporating a self-consistent thermal model  
592 into the inversion, projections may misrepresent the onset and extent of these dynamic  
593 instabilities. Our findings underscore that a fully coupled inversion framework would  
594 use not only surface velocity data but also incorporate direct or proxy observations of  
595 basal temperature and subglacial hydrology. Such an approach would better constrain  
596 the basal friction coefficient in a physically consistent manner, reducing the risk of  
597 producing nonphysical states. This integration is especially critical for projections of  
598 ice sheet evolution under climate change, as the dynamic response is sensitive to even  
599 small changes in basal conditions.

## 601 5. Conclusion

602 We propose a novel and rapid method to quantify the inconsistencies between  
603 modelled basal ice temperature and observed surface ice speed and assess the quality  
604 of ice sheet model simulation results without using subglacial observation data.  
605 Previously, it has been assumed that checking the quality of an ice sheet temperature  
606 model required in situ observations, whether from ice cores or geophysical techniques  
607 like ice penetrating radar. By using the ice temperature field to compute the rheology  
608 structure needed for a mechanical inversion and then quantifying the inconsistency  
609 between the inverted velocity field and the original ice temperature field, we are able

610 to use remotely sensed surface velocity observations as a check on the quality of  
611 modelled englacial temperatures. Given the challenges in acquiring subglacial data, our  
612 method can provide a streamlined and effective approach to evaluation.

613 We apply this method to the simulation results of Totten Glacier using a 3D full-  
614 Stokes model with 8 different GHF datasets. Assuming the inconsistencies are mainly  
615 due to unrealistic GHF datasets, we use the inconsistencies to assess the reliability of  
616 those GHF datasets. We compare our GHF ranking with that by Huang et al. (2024)  
617 which used specularity content to derive a two-sided constraint on the basal thermal  
618 state. We find that the top 4 and the bottom 4 GHFs are the same in the two studies,  
619 albeit with slight variations in ranking. Furthermore, we find that the simulations with  
620 all GHF datasets underestimate the basal ice temperature in a canyon on the western  
621 boundary of Totten Glacier, and we infer that the common high overheating  
622 inconsistencies with all the GHF datasets in the eastern Totten Glacier between 69°S  
623 and 72°S may be attributed to the unrealistically warm surface ice temperature used  
624 there in the model. While we demonstrate that this approach works on simulation results  
625 for Totten Glacier, testing of the method on other glaciers would be useful to assess if  
626 the approach is worthwhile for revealing ambiguous conflicts in observations and  
627 simulations.

628

629

630

631 *Data availability.* MEaSURES BedMachine Antarctica, version 2, is available at  
632 <https://doi.org/10.5067/E1QL9HFQ7A8M> (Morlighem, 2020). MEaSURES InSAR-  
633 Based Antarctic Ice Velocity Map, version 2, is available at  
634 <https://doi.org/10.5067/D7GK8F5J8M8R> (Rignot et al., 2017). MEaSURES Antarctic  
635 Boundaries for IPY 2007–2009 from Satellite Radar, version 2, is available at  
636 <https://doi.org/10.5067/AXE4121732AD> (Mouginot et al., 2017). ALBMAP v1 and the  
637 GHF dataset of Shapiro and Ritzwoller (2004) are available at  
638 <https://doi.org/10.1594/PANGAEA.734145> (Le Brocq et al., 2010b). The GHF dataset  
639 of An et al. (2015) is available at  
640 <http://www.seismolab.org/model/antarctica/lithosphere/AN1-HF.tar.gz> (last access: 11  
641 April 2023). The GHF dataset of Shen et al. (2020) is available at  
642 <https://sites.google.com/view/weisen/research-products?authuser=0> (last access: 11  
643 April 2023). The GHF dataset of Martos (2017) is available at  
644 <https://doi.org/10.1594/PANGAEA.882503>. The GHF dataset of Purucker (2012) is  
645 available at  
646 [https://core2.gsfc.nasa.gov/research/purucker/heatflux\\_mf7\\_foxmaule05.txt](https://core2.gsfc.nasa.gov/research/purucker/heatflux_mf7_foxmaule05.txt) (last  
647 access: 11 April 2023).

648

649 *Author contributions.* LZ and JCM conceived the study. LZ, MW, and JCM designed  
650 the methodology. JW and LZ analyzed the data and conducted visualization. JW  
651 and LZ wrote the original draft, and all the authors revised the paper.

652

653 *Competing interests.* The contact author has declared that none of the authors has any  
654 competing interests.

655

656 *Acknowledgements.* This work was supported by [National Natural Science Foundation](#)  
657 [of China \(grant no. 42576280\)](#)~~[National Key Research and Development Program](#)~~  
658 ~~[of China \(grant no. 2021YFB3900105\)](#)~~ and Academy of Finland (grant no.  
659 355572).

660

## 661 **References**

- 662 Albrecht, T., Winkelmann, R., and Levermann, A.: Glacial-cycle simulations of the Antarctic Ice  
663 Sheet with the Parallel Ice Sheet Model (PISM) – Part 1: Boundary conditions and climatic  
664 forcing, *The Cryosphere*, 14, 599–632, <https://doi.org/10.5194/tc-14-599-2020>, 2020.
- 665 An, M., Wiens, D. A., Zhao, Y., Feng, M., Nyblade, A., Kanao, M., Li, Y., Maggi, A., and L  v  que,  
666 J.: Temperature, lithosphere-asthenosphere boundary, and heat flux beneath the Antarctic Plate  
667 inferred from seismic velocities, *J. Geophys. Res. Solid Earth*, 120, 8720–8742,  
668 <https://doi.org/10.1002/2015JB011917>, 2015.
- 669 Artemieva, I. M.: Antarctica ice sheet basal melting enhanced by high mantle heat, *Earth-Sci. Rev.*,  
670 226, 103954, <https://doi.org/10.1016/j.earscirev.2022.103954>, 2022.
- 671 Azuma, N. and Higashi, A.: Formation Processes of Ice Fabric Pattern in Ice Sheets, *Ann. Glaciol.*,  
672 6, 130–134, <https://doi.org/10.3189/1985AoG6-1-130-134>, 1985.
- 673 Benn, D. I., Luckman, A.,   str  m, J. A., Crawford, A. J., Cornford, S. L., Bevan, S. L., Zwinger, T.,  
674 Gladstone, R., Alley, K., Pettit, E., and Bassis, J.: Rapid fragmentation of Thwaites Eastern Ice  
675 Shelf, *The Cryosphere*, 16, 2545–2564, <https://doi.org/10.5194/tc-16-2545-2022>, 2022.
- 676 Brondex, J., Gagliardini, O., Gillet-Chaulet, F., and Durand, G.: Sensitivity of grounding line  
677 dynamics to the choice of the friction law, *J. Glaciol.*, 63, 854–866,  
678 <https://doi.org/10.1017/jog.2017.51>, 2017.
- 679 Brondex, J., Gillet-Chaulet, F., and Gagliardini, O.: Sensitivity of centennial mass loss projections  
680 of the Amundsen basin to the friction law, *The Cryosphere*, 13, 177–195,  
681 <https://doi.org/10.5194/tc-13-177-2019>, 2019.
- 682 Budd, W. F. and Jacka, T. H.: A review of ice rheology for ice sheet modelling, *Cold Reg. Sci.*  
683 *Technol.*, 16, 107–144, [https://doi.org/10.1016/0165-232X\(89\)90014-1](https://doi.org/10.1016/0165-232X(89)90014-1), 1989.
- 684 Budd, W. F., Keage, P. L., and Blundy, N. A.: Empirical Studies of Ice Sliding, *J. Glaciol.*, 23, 157–  
685 170, <https://doi.org/10.3189/S0022143000029804>, 1979.
- 686 Burton-Johnson, A., Dziadek, R., and Martin, C.: Review article: Geothermal heat flow in  
687 Antarctica: current and future directions, *The Cryosphere*, 14, 3843–3873,  
688 <https://doi.org/10.5194/tc-14-3843-2020>, 2020.



689 Choi, Y., Seroussi, H., Morlighem, M., Schlegel, N.-J., and Gardner, A.: Impact of time-dependent  
690 data assimilation on ice flow model initialization and projections: a case study of Kjer Glacier,  
691 Greenland, *The Cryosphere*, 17, 5499–5517, <https://doi.org/10.5194/tc-17-5499-2023>, 2023.

692 Cornford, S. L., Martin, D. F., Payne, A. J., Ng, E. G., Le Brocq, A. M., Gladstone, R. M., Edwards,  
693 T. L., Shannon, S. R., Agosta, C., Van Den Broeke, M. R., Hellmer, H. H., Krinner, G.,  
694 Ligtenberg, S. R. M., Timmermann, R., and Vaughan, D. G.: Century-scale simulations of the  
695 response of the West Antarctic Ice Sheet to a warming climate, *The Cryosphere*, 9, 1579–1600,  
696 <https://doi.org/10.5194/tc-9-1579-2015>, 2015.

697 Dow, C. F., McCormack, F. S., Young, D. A., Greenbaum, J. S., Roberts, J. L., and Blankenship, D.  
698 D.: Totten Glacier subglacial hydrology determined from geophysics and modeling, *Earth  
699 Planet. Sci. Lett.*, 531, 115961, <https://doi.org/10.1016/j.epsl.2019.115961>, 2020.

700 Dziadek, R., Gohl, K., Diehl, A., and Kaul, N.: Geothermal heat flux in the Amundsen Sea sector  
701 of West Antarctica: New insights from temperature measurements, depth to the bottom of the  
702 magnetic source estimation, and thermal modeling, *Geochem. Geophys. Geosystems*, 18,  
703 2657–2672, <https://doi.org/10.1002/2016GC006755>, 2017.

704 Fisher, A. T., Mankoff, K. D., Tulaczyk, S. M., Tyler, S. W., and Foley, N.: High geothermal heat  
705 flux measured below the West Antarctic Ice Sheet, *Sci. Adv.*, 1(6), e1500093,  
706 <https://doi.org/10.1126/sciadv.1500093>, 2015.

707 Fowler, A. C.: A theoretical treatment of the sliding of glaciers in the absense of cavitation, *Philos.  
708 Trans. R. Soc. Lond. Ser. Math. Phys. Sci.*, 298, 637–681,  
709 <https://doi.org/10.1098/rsta.1981.0003>, 1981.

710 Fujita, S. and Mae, S.: Strain in the ice sheet deduced from the crystal-orientation fabrics from bare  
711 icefields adjacent to the Sør-Rondane Mountains, Dronning Maud Land, East Antarctica, *J.  
712 Glaciol.*, 40, 135–139, <https://doi.org/10.3189/S0022143000003907>, 1994.

713 Gagliardini, O., Cohen, D., Råback, P., and Zwinger, T.: Finite-element modeling of subglacial  
714 cavities and related friction law, *J. Geophys. Res. Earth Surf.*, 112, F02027,  
715 <https://doi.org/10.1029/2006JF000576>, 2007.

716 Gerber, T. A., Lilien, D. A., Rathmann, N. M., Franke, S., Young, T. J., Valero-Delgado, F., Ershadi,  
717 M. R., Drews, R., Zeising, O., Humbert, A., Stoll, N., Weikusat, I., Grinsted, A., Hvidberg, C.  
718 S., Jansen, D., Miller, H., Helm, V., Steinhage, D., O’Neill, C., Paden, J., Gogineni, S. P., Dahl-  
719 Jensen, D., and Eisen, O.: Crystal orientation fabric anisotropy causes directional hardening of  
720 the Northeast Greenland Ice Stream, *Nat. Commun.*, 14, 2653, [https://doi.org/10.1038/s41467-  
721 023-38139-8](https://doi.org/10.1038/s41467-023-38139-8), 2023.

722 Gillet-Chaulet, F., Gagliardini, O., Seddik, H., Nodet, M., Durand, G., Ritz, C., Zwinger, T., Greve,  
723 R., and Vaughan, D. G.: Greenland ice sheet contribution to sea-level rise from a new-  
724 generation ice-sheet model, *The Cryosphere*, 6, 1561–1576, [https://doi.org/10.5194/tc-6-1561-  
725 2012](https://doi.org/10.5194/tc-6-1561-2012), 2012.

726 Gladstone, R., Schäfer, M., Zwinger, T., Gong, Y., Strozzi, T., Mottram, R., Boberg, F., and Moore,  
727 J. C.: Importance of basal processes in simulations of a surging Svalbard outlet glacier, *The  
728 Cryosphere*, 8, 1393–1405, <https://doi.org/10.5194/tc-8-1393-2014>, 2014.

729 Greenbaum, J. S., Blankenship, D. D., Young, D. A., Richter, T. G., Roberts, J. L., Aitken, A. R. A.,  
730 Legresy, B., Schroeder, D. M., Warner, R. C., van Ommen, T. D., and Siegert, M. J.: Ocean  
731 access to a cavity beneath Totten Glacier in East Antarctica, *Nat. Geosci.*, 8, 294–298,  
732 <https://doi.org/10.1038/ngeo2388>, 2015.

733 Haeger, C., Petrunin, A. G., and Kaban, M. K.: Geothermal Heat Flow and Thermal Structure of the  
734 Antarctic Lithosphere, *Geochem. Geophys. Geosystems*, 23, e2022GC010501,  
735 <https://doi.org/10.1029/2022GC010501>, 2022.

736 Huang, Y., Zhao, L., Wolovick, M., Ma, Y., and Moore, J. C.: Using specularity content to evaluate  
737 eight geothermal heat flow maps of Totten Glacier, *The Cryosphere*, 18, 103–119,  
738 <https://doi.org/10.5194/tc-18-103-2024>, 2024.

739 Jordan, T. M., Martín, C., Brisbourne, A. M., Schroeder, D. M., and Smith, A. M.: Radar  
740 Characterization of Ice Crystal Orientation Fabric and Anisotropic Viscosity Within an  
741 Antarctic Ice Stream, *J. Geophys. Res. Earth Surf.*, 127, e2022JF006673,  
742 <https://doi.org/10.1029/2022JF006673>, 2022.

743 Kamb, B.: Sliding motion of glaciers: Theory and observation, *Rev. Geophys.*, 8, 673–728,  
744 <https://doi.org/10.1029/RG008i004p00673>, 1970.

745 Kang, H., Zhao, L., Wolovick, M., and Moore, J. C.: Evaluation of six geothermal heat flux maps  
746 for the Antarctic Lambert–Amery glacial system, *The Cryosphere*, 16, 3619–3633,  
747 <https://doi.org/10.5194/tc-16-3619-2022>, 2022.

748 Kim, B.-H., Seo, K.-W., Lee, C.-K., Kim, J.-S., Lee, W. S., Jin, E. K., and Van Den Broeke, M.:  
749 Partitioning the drivers of Antarctic glacier mass balance (2003–2020) using satellite  
750 observations and a regional climate model, *Proc. Natl. Acad. Sci.*, 121, e2322622121,  
751 <https://doi.org/10.1073/pnas.2322622121>, 2024.

752 Larour, E., Seroussi, H., Morlighem, M., and Rignot, E.: Continental scale, high order, high spatial  
753 resolution, ice sheet modeling using the Ice Sheet System Model (ISSM), *J. Geophys. Res.*,  
754 117, F01022, <https://doi.org/10.1029/2011JF002140>, 2012.

755 Le Brocq, A. M., Payne, A. J., and Vieli, A.: An improved Antarctic dataset for high resolution  
756 numerical ice sheet models (ALBMAP v1), *Earth Syst. Sci. Data*, 2, 247–260,  
757 <https://doi.org/10.5194/essd-2-247-2010>, 2010.

758 Lipscomb, W. H., Leguy, G. R., Jourdain, N. C., Asay-Davis, X., Seroussi, H., and Nowicki, S.:  
759 ISMIP6-based projections of ocean-forced Antarctic Ice Sheet evolution using the  
760 Community Ice Sheet Model, *The Cryosphere*, 15, 633–661, <https://doi.org/10.5194/tc-15-633-2021>, 2021.

762 Lhermitte, S., Sun, S., Shuman, C., Wouters, B., Pattyn, F., Wuite, J., Berthier, E., and Nagler, T.:  
763 Damage accelerates ice shelf instability and mass loss in Amundsen Sea Embayment, *Proc.*  
764 *Natl. Acad. Sci.*, 117, 24735–24741, <https://doi.org/10.1073/pnas.1912890117>, 2020.

765 Lösing, M. and Ebbing, J.: Predicting Geothermal Heat Flow in Antarctica With a Machine Learning  
766 Approach, *J. Geophys. Res. Solid Earth*, 126, e2020JB021499,  
767 <https://doi.org/10.1029/2020JB021499>, 2021.

768 MacAyeal, D. R.: A tutorial on the use of control methods in ice-sheet modeling, *J. Glaciol.*, 39, 91–

769 98, <https://doi.org/10.3189/S0022143000015744>, 1993.

770 Martín, C., Gudmundsson, G. H., Pritchard, H. D., and Gagliardini, O.: On the effects of anisotropic  
771 rheology on ice flow, internal structure, and the age-depth relationship at ice divides, *J.*  
772 *Geophys. Res. Earth Surf.*, 114, F04001, <https://doi.org/10.1029/2008JF001204>, 2009.

773 Martos, Y. M., Catalán, M., Jordan, T. A., Golynsky, A., Golynsky, D., Eagles, G., and Vaughan, D.  
774 G.: Heat Flux Distribution of Antarctica Unveiled, *Geophys. Res. Lett.*, 44, 11,417–11,426,  
775 <https://doi.org/10.1002/2017GL075609>, 2017.

776 Maule, C. F., Purucker, M. E., Olsen, N., and Mosegaard, K.: Heat Flux Anomalies in Antarctica  
777 Revealed by Satellite Magnetic Data, *Science*, 309, 464–467,  
778 <https://doi.org/10.1126/science.1106888>, 2005.

779 McCormack, F. S., Roberts, J. L., Dow, C. F., Stål, T., Halpin, J. A., Reading, A. M., and Siegert, M.  
780 J.: Fine-Scale Geothermal Heat Flow in Antarctica Can Increase Simulated Subglacial Melt  
781 Estimates, *Geophys. Res. Lett.*, 49, e2022GL098539, <https://doi.org/10.1029/2022GL098539>,  
782 2022.

783 Morlighem, M., Seroussi, H., Larour, E., and Rignot, E.: Inversion of basal friction in Antarctica  
784 using exact and incomplete adjoints of a higher-order model, *J. Geophys. Res. Earth Surf.*, 118,  
785 1746–1753, <https://doi.org/10.1002/jgrf.20125>, 2013.

786 Morlighem, M., Rignot, E., Binder, T., Blankenship, D., Drews, R., Eagles, G., Eisen, O., Ferraccioli,  
787 F., Forsberg, R., Fretwell, P., Goel, V., Greenbaum, J. S., Gudmundsson, H., Guo, J., Helm, V.,  
788 Hofstede, C., Howat, I., Humbert, A., Jokat, W., Karlsson, N. B., Lee, W. S., Matsuoka, K.,  
789 Millan, R., Mouginot, J., Paden, J., Pattyn, F., Roberts, J., Rosier, S., Ruppel, A., Seroussi, H.,  
790 Smith, E. C., Steinhage, D., Sun, B., Broeke, M. R. V. D., Ommen, T. D. V., Wessem, M. V.,  
791 and Young, D. A.: Deep glacial troughs and stabilizing ridges unveiled beneath the margins of  
792 the Antarctic ice sheet, *Nat. Geosci.*, 13, 132–137, [https://doi.org/10.1038/s41561-019-0510-](https://doi.org/10.1038/s41561-019-0510-8)  
793 8, 2020.

794 Nye, J. F.: Glacier sliding without cavitation in a linear viscous approximation, *Proc. R. Soc. Lond.*  
795 *Math. Phys. Sci.*, 315, 381–403, <https://doi.org/10.1098/rspa.1970.0050>, 1970.

796 Park, I.-W., Jin, E. K., Morlighem, M., and Lee, K.-K.: Impact of boundary conditions on the  
797 modeled thermal regime of the Antarctic ice sheet, *The Cryosphere*, 18, 1139–1155,  
798 <https://doi.org/10.5194/tc-18-1139-2024>, 2024.

799 Paterson, W. S. B.: Why ice-age ice is sometimes “soft,” *Cold Reg. Sci. Technol.*, 20, 75–98,  
800 [https://doi.org/10.1016/0165-232X\(91\)90058-O](https://doi.org/10.1016/0165-232X(91)90058-O), 1991.

801 Pattyn, F.: Sea-level response to melting of Antarctic ice shelves on multi-centennial timescales  
802 with the fast Elementary Thermomechanical Ice Sheet model (f.ETISH v1.0), *The*  
803 *Cryosphere*, 11, 1851–1878, <https://doi.org/10.5194/tc-11-1851-2017>, 2017.

804 Payne, A. J., Nowicki, S., Abe-Ouchi, A., Agosta, C., Alexander, P., Albrecht, T., Asay-Davis, X.,  
805 Aschwanden, A., Barthel, A., Bracegirdle, T. J., Calov, R., Chambers, C., Choi, Y., Cullather,  
806 R., Cuzzone, J., Dumas, C., Edwards, T. L., Felikson, D., Fettweis, X., Galton-Fenzi, B. K.,  
807 Goelzer, H., Gladstone, R., Golledge, N. R., Gregory, J. M., Greve, R., Hattermann, T.,  
808 Hoffman, M. J., Humbert, A., Huybrechts, P., Jourdain, N. C., Kleiner, T., Munneke, P. K.,

809 Larour, E., Le Clec'H, S., Lee, V., Leguy, G., Lipscomb, W. H., Little, C. M., Lowry, D. P.,  
810 Morlighem, M., Nias, I., Pattyn, F., Pelle, T., Price, S. F., Quiquet, A., Reese, R., Rückamp, M.,  
811 Schlegel, N., Seroussi, H., Shepherd, A., Simon, E., Slater, D., Smith, R. S., Straneo, F., Sun,  
812 S., Tarasov, L., Trusel, L. D., Van Breedam, J., Van De Wal, R., Van Den Broeke, M.,  
813 Winkelmann, R., Zhao, C., Zhang, T., and Zwinger, T.: Future Sea Level Change Under  
814 Coupled Model Intercomparison Project Phase 5 and Phase 6 Scenarios From the Greenland  
815 and Antarctic Ice Sheets, *Geophys. Res. Lett.*, 48, e2020GL091741,  
816 <https://doi.org/10.1029/2020GL091741>, 2021.

817 Peyaud, V., Bouchayer, C., Gagliardini, O., Vincent, C., Gillet-Chaulet, F., Six, D., and Laarman,  
818 O.: Numerical modeling of the dynamics of the Mer de Glace glacier, French Alps: comparison  
819 with past observations and forecasting of near-future evolution, *The Cryosphere*, 14, 3979–  
820 3994, <https://doi.org/10.5194/tc-14-3979-2020>, 2020.

821 Pittard, M. L., Roberts, J. L., Galton-Fenzi, B. K., and Watson, C. S.: Sensitivity of the Lambert-  
822 Amery glacial system to geothermal heat flux, *Ann. Glaciol.*, 57, 56 – 68,  
823 <https://doi.org/10.1017/aog.2016.26>, 2016.

824 Pollard, D. and DeConto, R. M.: A simple inverse method for the distribution of basal sliding  
825 coefficients under ice sheets, applied to Antarctica, *The Cryosphere*, 6, 953–971,  
826 <https://doi.org/10.5194/tc-6-953-2012>, 2012.

827 Pritchard, H. D., Arthern, R. J., Vaughan, D. G., and Edwards, L. A.: Extensive dynamic thinning  
828 on the margins of the Greenland and Antarctic ice sheets, *Nature*, 461, 971–975,  
829 <https://doi.org/10.1038/nature08471>, 2009.

830 Pritchard, H.D., Fretwell, P.T., Fremant, A.C. et al. Bedmap3 updated ice bed, surface and thickness  
831 gridded datasets for Antarctica. *Sci Data* 12, 414 (2025). [https://doi.org/10.1038/s41597-025-](https://doi.org/10.1038/s41597-025-04672-y)  
832 [04672-y](https://doi.org/10.1038/s41597-025-04672-y)

833 Purucker, M.: Geothermal heat flux data set based on low resolution observations collected by the  
834 CHAMP satellite between 2000 and 2010, and produced from the MF-6 model following the  
835 technique described in Fox Maule et al. (2005), Interactive System for Ice sheet Simulation  
836 [data set], [https://core2.gsfc.nasa.gov/research/purucker/heatflux\\_mf7\\_foxmaule05.txt](https://core2.gsfc.nasa.gov/research/purucker/heatflux_mf7_foxmaule05.txt) (last  
837 access: 24 December 2023), 2012.

838 Rathmann, N. M. and Lilien, D. A.: Inferred basal friction and mass flux affected by crystal-  
839 orientation fabrics, *J. Glaciol.*, 68, 236–252, <https://doi.org/10.1017/jog.2021.88>, 2022.

840 Reading, A. M.: Antarctic geothermal heat flow and its implications for tectonics and ice sheets,  
841 *Nat. Rev. Earth Environ.*, 3, 814–831, <https://doi.org/10.1038/s43017-022-00348-y>, 2022.

842 Reese, R., Garbe, J., Hill, E. A., Urruty, B., Naughten, K. A., Gagliardini, O., Durand, G., Gillet-  
843 Chaulet, F., Gudmundsson, G. H., Chandler, D., Langebroek, P. M., and Winkelmann, R.: The  
844 stability of present-day Antarctic grounding lines – Part 2: Onset of irreversible retreat of  
845 Amundsen Sea glaciers under current climate on centennial timescales cannot be excluded,  
846 *The Cryosphere*, 17, 3761–3783, <https://doi.org/10.5194/tc-17-3761-2023>, 2023.

847 Ross, N., Bingham, R. G., Corr, H. F. J., Ferraccioli, F., Jordan, T. A., Le Brocq, A., Rippin, D. M.,  
848 Young, D., Blankenship, D. D., and Siegert, M. J.: Steep reverse bed slope at the grounding

849 line of the Weddell Sea sector in West Antarctica, *Nat. Geosci.*, 5, 393–396,  
850 <https://doi.org/10.1038/ngeo1468>, 2012.

851 Rignot, E., Mouginot, J., and Scheuchl, B.: MEaSURES InSAR-Based Antarctica Ice Velocity Map,  
852 Version 2, Boulder, Colorado USA, NASA National Snow and Ice Data Center Distributed  
853 Active Archive Center [data Set], <https://doi.org/10.5067/D7GK8F5J8M8R>, 2017.

854 Rignot, E., Mouginot, J., Scheuchl, B., Van Den Broeke, M., Van Wessem, M. J., and Morlighem,  
855 M.: Four decades of Antarctic Ice Sheet mass balance from 1979–2017, *Proc. Natl. Acad. Sci.*,  
856 116, 1095–1103, <https://doi.org/10.1073/pnas.1812883116>, 2019.

857 Schannwell, C., Drews, R., Ehlers, T. A., Eisen, O., Mayer, C., Malinen, M., Smith, E. C., and  
858 Eisermann, H.: Quantifying the effect of ocean bed properties on ice sheet geometry over 40  
859 000 years with a full-Stokes model, *The Cryosphere*, 14, 3917–3934,  
860 <https://doi.org/10.5194/tc-14-3917-2020>, 2020.

861 Schoof, C.: On the mechanics of ice-stream shear margins, *J. Glaciol.*, 50, 208–218,  
862 <https://doi.org/10.3189/172756504781830024>, 2004.

863 Schoof, C.: The effect of cavitation on glacier sliding, *Proc. R. Soc. Math. Phys. Eng. Sci.*, 461,  
864 609–627, <https://doi.org/10.1098/rspa.2004.1350>, 2005.

865 Schroeder, D. M., Blankenship, D. D., and Young, D. A.: Evidence for a water system transition  
866 beneath Thwaites Glacier, West Antarctica, *Proc. Natl. Acad. Sci.*, 110, 12225–12228,  
867 <https://doi.org/10.1073/pnas.1302828110>, 2013.

868 Schroeder, D. M., Blankenship, D. D., Raney, R. K., and Grima, C.: Estimating Subglacial Water  
869 Geometry Using Radar Bed Echo Specularity: Application to Thwaites Glacier, West  
870 Antarctica, *IEEE Geosci. Remote Sens. Lett.*, 12, 443–447,  
871 <https://doi.org/10.1109/LGRS.2014.2337878>, 2015.

872 Seroussi, H., Nowicki, S., Simon, E., Abe-Ouchi, A., Albrecht, T., Brondex, J., Cornford, S., Dumas,  
873 C., Gillet-Chaulet, F., Goelzer, H., Gollede, N. R., Gregory, J. M., Greve, R., Hoffman, M. J.,  
874 Humbert, A., Huybrechts, P., Kleiner, T., Larour, E., Leguy, G., Lipscomb, W. H., Lowry, D.,  
875 Mengel, M., Morlighem, M., Pattyn, F., Payne, A. J., Pollard, D., Price, S. F., Quiquet, A.,  
876 Reerink, T. J., Reese, R., Rodehacke, C. B., Schlegel, N.-J., Shepherd, A., Sun, S., Sutter, J.,  
877 Van Breedam, J., Van De Wal, R. S. W., Winkelmann, R., and Zhang, T.: initMIP-Antarctica:  
878 an ice sheet model initialization experiment of ISMIP6, *The Cryosphere*, 13, 1441–1471,  
879 <https://doi.org/10.5194/tc-13-1441-2019>, 2019.

880 Shackleton, C., Matsuoka, K., Moholdt, G., Van Liefferinge, B., and Paden, J.: Stochastic  
881 Simulations of Bed Topography Constrain Geothermal Heat Flow and Subglacial Drainage  
882 Near Dome Fuji, East Antarctica, *J. Geophys. Res. Earth Surf.*, 128, e2023JF007269,  
883 <https://doi.org/10.1029/2023JF007269>, 2023.

884 Shapiro, N.: Inferring surface heat flux distributions guided by a global seismic model: particular  
885 application to Antarctica, *Earth Planet. Sci. Lett.*, 223, 213–224,  
886 <https://doi.org/10.1016/j.epsl.2004.04.011>, 2004.

887 Shen, W., Wiens, D. A., Lloyd, A. J., and Nyblade, A. A.: A Geothermal Heat Flux Map of Antarctica  
888 Empirically Constrained by Seismic Structure, *Geophys. Res. Lett.*, 47, e2020GL086955,

889 <https://doi.org/10.1029/2020GL086955>, 2020.

890 Siahayan, A., Smith, R. S., Holland, P. R., Jenkins, A., Gregory, J. M., Lee, V., Mathiot, P., Payne, A.  
891 J., Ridley, J. K., and Jones, C. G.: The Antarctic contribution to 21st-century sea-level rise  
892 predicted by the UK Earth System Model with an interactive ice sheet, *The Cryosphere*, 16,  
893 4053 – 4086, <https://doi.org/10.5194/tc-16-4053-2022>, 2022.

894 Smith-Johnsen, S., Schlegel, N. -J., De Fleurian, B., and Nisancioglu, K. H.: Sensitivity of the  
895 Northeast Greenland Ice Stream to Geothermal Heat, *J. Geophys. Res. Earth Surf.*, 125,  
896 e2019JF005252, <https://doi.org/10.1029/2019JF005252>, 2020.

897 Stål, T., Reading, A. M., Halpin, J. A., and Whittaker, J. M.: Antarctic Geothermal Heat Flow Model:  
898 Aq1, *Geochem. Geophys. Geosystems*, 22, e2020GC009428,  
899 <https://doi.org/10.1029/2020GC009428>, 2021.

900 Sun, S., Cornford, S. L., Moore, J. C., Gladstone, R., and Zhao, L.: Ice shelf fracture  
901 parameterization in an ice sheet model, *The Cryosphere*, 11, 2543–2554,  
902 <https://doi.org/10.5194/tc-11-2543-2017>, 2017.

903 Tsai, V. C., Stewart, A. L., and Thompson, A. F.: Marine ice-sheet profiles and stability under  
904 Coulomb basal conditions, *J. Glaciol.*, 61, 205–215, <https://doi.org/10.3189/2015JoG14J221>,  
905 2015.

906 Van Liefferinge, B., Pattyn, F., Cavitte, M. G. P., Karlsson, N. B., Young, D. A., Sutter, J., and Eisen,  
907 O.: Promising Oldest Ice sites in East Antarctica based on thermodynamical modelling, *The*  
908 *Cryosphere*, 12, 2773–2787, <https://doi.org/10.5194/tc-12-2773-2018>, 2018.

909 Weertman, J.: On the Sliding of Glaciers, *J. Glaciol.*, 3, 33–38,  
910 <https://doi.org/10.3189/S0022143000024709>, 1957.

911 Young, D. A., Schroeder, D. M., Blankenship, D. D., Kempf, S. D., and Quartini, E.: The distribution  
912 of basal water between Antarctic subglacial lakes from radar sounding, *Philos. Trans. R. Soc.*  
913 *Math. Phys. Eng. Sci.*, 374, 20140297, <https://doi.org/10.1098/rsta.2014.0297>, 2016.

914 Zhao, C., Gladstone, R. M., Warner, R. C., King, M. A., Zwinger, T., and Morlighem, M.: Basal  
915 friction of Fleming Glacier, Antarctica – Part 1: Sensitivity of inversion to temperature and  
916 bedrock uncertainty, *The Cryosphere*, 12, 2637–2652, [https://doi.org/10.5194/tc-12-2637-](https://doi.org/10.5194/tc-12-2637-2018)  
917 2018, 2018a.

918 Zhao, L., Moore, J. C., Sun, B., Tang, X., and Guo, X.: Where is the 1-million-year-old ice at Dome  
919 A?, *The Cryosphere*, 12, 1651–1663, <https://doi.org/10.5194/tc-12-1651-2018>, 2018b.

920 Zhang, X., Dong, X., Zeng, J, Hou, S., Smeets, P., Reijmer, C. H., and Wang, Y., Spatiotemporal  
921 Reconstruction of Antarctic Near-Surface Air Temperature from MODIS Observations, *J.*  
922 *Clim.*, 35, 5537-5553, 2022.

923 Zwinger, T., Schäfer, M., Martín, C., and Moore, J. C.: Influence of anisotropy on velocity and age  
924 distribution at Scharffenbergbotnen blue ice area, *The Cryosphere*, 8, 607–621,  
925 <https://doi.org/10.5194/tc-8-607-2014>, 2014.

926